

## Be DOPING OF MBE-GROWN InP NANOWIRES

# Be DOPING OF MBE-GROWN InP NANOWIRES

By

ROBIN JENNIFER YEE, B.Eng.Society

A Thesis

Submitted to the School of Graduate Studies

in Partial Fulfilment of the Requirements

for the Degree

Master of Applied Science

McMaster University

© Copyright by Robin Jennifer Yee, August 2013

**MASTER OF APPLIED SCIENCE (2013)**  
**(Department of Engineering Physics)**

**McMaster University**  
**Hamilton, Ontario**

TITLE: Be-Doping of MBE-Grown InP Nanowires

AUTHOR: Robin Jennifer Yee, B.Eng.Society (McMaster University)

SUPERVISOR: Dr. Ray R. LaPierre

NUMBER OF PAGES: xiii, 66

## ABSTRACT

Be-doped InP nanowires were grown by the gold-assisted vapour-liquid-solid mechanism in a gas source molecular beam epitaxy system. The nanowires were characterized by scanning and transmission electron microscopy. With increased doping, the dependence of the length on diameter  $[L(D)]$  underwent an unusual transition from the diffusion-limited  $1/D^2$  relationship to one that increased before saturating. Doping influences on crystal structure and radial growth have been reported previously, but in the absence of these effects it is speculated that the beryllium introduces an increase in the steady-state chemical potential of the catalyst, and a barrier to nucleation. A model is presented relating the diffusion- and nucleation-limited regimes.

Additionally, the progressive increase of dopant incorporation was verified by secondary ion mass spectrometry. Samples were transformed into a "bulk-like" material by spin-coating with cyclohexane to enable depth profiling. Carrier concentrations were inferred through comparison with a thin film reference, and agreed in order of magnitude with the nominal doping values.

Dopant activation was investigated through micro-photoluminescence experiments, and showed peak emissions between 1.49 eV and 1.50 eV for undoped samples, transitioning with increased doping to 1.45-1.46 eV. The difference between the dominant peak energies was consistent with differences

reported for comparable epitaxially-grown thin film samples. Bandgap narrowing was also observed at high levels of doping, and was consistent with theoretical predictions.

As a whole, the work presented here provides a different perspective on the effects of doping on nanowire growth, demonstrated through the specific system of Be-doped InP. The findings have implications for predictable and consistent nanowire device design, and suggestions for avenues of future research are provided.

## ACKNOWLEDGEMENTS

The completion of this thesis would not have been possible without the appreciable assistance of my supervisor and research group. My most sincere thanks go to **Dr. Ray LaPierre** for his support and encouragement in this endeavour. Thanks to your patient supervision and guidance, the last two years have been a challenging and satisfying experience for which I am very grateful. To **the members of Team LaPierre**: I could not have asked for more exemplary colleagues. Special thanks are owed to Chris, Paul, Andrew, and Jonathan for experimental and imaging assistance; Sandra for invaluable discussions; and everyone for sharing the adventure along the way – “If we knew what we were doing, it wouldn’t be called Research.”

I also wish to thank:

- **the CCEM staff**, especially Fred Pearson, Carmen Andrei, and Andy Duft for training and guidance on the electron microscopes;
- **the CEDT staff**, particularly Doris Stevanovic and Shahram Tavakoli for cleanroom sample preparation and MBE growths;
- **V.G. Dubrovskii** of St. Petersburg Academic University for his collaboration developing the nanowire growth model;
- **Gary Good** of Surface Science Western for SIMS analysis and discussion;

- **the Engineering Physics Department and CEDT administrative staff**, especially Marilyn, Linda, Samantha, and Fran, for friendly assistance with countless questions over the years;
- and **NSERC** for the financial support that allowed me to pursue this research.

Finally, many, many thanks are owed to those who have been my constants throughout this journey: **my mum, dad, brother, the lovely Eigenhouse ladies**, and **Naomi**. For your understanding and support; good company and companionship; and the innumerable ways you bring joy to my life, I owe you all a world of thanks. Much love, and here's to many more adventures to come.

# TABLE OF CONTENTS

<b>ABSTRACT</b>	<b>III</b>
<b>ACKNOWLEDGEMENTS</b>	<b>V</b>
<b>TABLE OF CONTENTS</b>	<b>VII</b>
<b>LIST OF FIGURES</b>	<b>IX</b>
<b>LIST OF TABLES</b>	<b>XI</b>
<b>LIST OF ABBREVIATIONS</b>	<b>XII</b>
<b>DECLARATION OF ACADEMIC ACHIEVEMENT</b>	<b>XIII</b>

## **CHAPTER 1 INTRODUCTION** **1**

<b>1.1 VLS NANOWIRE GROWTH</b>	<b>2</b>
<b>1.2 MOTIVATIONS FOR PRESENT WORK</b>	<b>6</b>
<b>1.3 THESIS OVERVIEW</b>	<b>7</b>

## **CHAPTER 2 GROWTH AND CHARACTERIZATION TECHNIQUES** **9**

<b>2.1 MOLECULAR BEAM EPITAXY</b>	<b>9</b>
<b>2.2 SAMPLE PREPARATION</b>	<b>12</b>
<b>2.3 ELECTRON MICROSCOPY</b>	<b>13</b>
2.3.1 SCANNING ELECTRON MICROSCOPY	14
2.3.2 TRANSMISSION ELECTRON MICROSCOPY	16
<b>2.4 SECONDARY ION MASS SPECTROMETRY</b>	<b>18</b>
<b>2.5 MICRO-PHOTOLUMINESCENCE SPECTROSCOPY</b>	<b>19</b>

<b><u>CHAPTER 3 EFFECTS OF BE-DOPING ON INP NANOWIRE GROWTH</u></b>	<b>23</b>
<b>3.1 INTRODUCTION</b>	<b>23</b>
<b>3.2 EXPERIMENTAL DETAILS</b>	<b>24</b>
<b>3.3 RESULTS AND DISCUSSION</b>	<b>25</b>
<b>3.4 MODEL OF LENGTH DEPENDENCE ON DIAMETER</b>	<b>32</b>
<b>3.5 CHAPTER SUMMARY</b>	<b>36</b>
<b><u>CHAPTER 4 COMPOSITIONAL CHARACTERIZATION</u></b>	<b>38</b>
<b>4.1 INTRODUCTION</b>	<b>38</b>
<b>4.2 EXPERIMENTAL DETAILS</b>	<b>38</b>
<b>4.3 RESULTS</b>	<b>40</b>
<b>4.4 DISCUSSION</b>	<b>45</b>
<b>4.5 CHAPTER SUMMARY</b>	<b>46</b>
<b><u>CHAPTER 5 OPTICAL CHARACTERIZATION ANALYSIS</u></b>	<b>48</b>
<b>5.1 INTRODUCTION</b>	<b>48</b>
<b>5.2 EXPERIMENTAL DETAILS</b>	<b>49</b>
<b>5.3 RESULTS</b>	<b>50</b>
<b>5.4 DISCUSSION</b>	<b>52</b>
<b>5.5 CHAPTER SUMMARY</b>	<b>55</b>
<b><u>CHAPTER 6 CONCLUSIONS AND FUTURE WORK</u></b>	<b>57</b>
<b>6.1 THESIS SUMMARY</b>	<b>57</b>
<b>6.2 FUTURE WORK</b>	<b>59</b>
<b><u>REFERENCES</u></b>	<b>61</b>

## LIST OF FIGURES

**Figure 1.1: The VLS process. a) A catalyst material (i.e. gold) is deposited onto the growth substrate. b) The catalyst is heated and assembles into nanoparticles. c) Growth species (here, III-V elements) introduced in vapour phase alloy with the liquid droplets. d) Once the alloyed droplet is supersaturated, the growth material precipitates at the solid-liquid interface. .... 3**

**Figure 1.2: In addition to (A) direct impingement on the droplet, systems with non-negligible diffusion lengths ( $\lambda$ ) must account for diffusion from (B) sidewalls and (C) the substrate collection area. .... 4**

**Figure 2.1: Diagram of the GS-MBE deposition chamber operated by the CEDT. Image used with permission from [30]. .... 11**

**Figure 2.2: Layout of the micro-photoluminescence system used to optically characterize nanowires. Image used with permission from [30]. .... 21**

**Figure 3.1: Tilted view ( $45^\circ$ ) SEM images of (a) sample A1, undoped, (b) sample A2, Be doping= $10^{18} \text{ cm}^{-3}$ , and (c) sample A3, Be doping= $2 \times 10^{19} \text{ cm}^{-3}$ . Scale bars indicate  $1 \mu\text{m}$ . .... 26**

**Figure 3.2: TEM image of typical nanowire from sample A3. Inset shows SAD pattern indicating the wurtzite crystal structure. .... 27**

**Figure 3.3: Length versus diameter for different Be doped InP nanowires (sample A1: undoped, sample A2:  $10^{18} \text{ cm}^{-3}$ , sample A3:  $2 \times 10^{19} \text{ cm}^{-3}$ ). Experimental data (symbols) are fitted by Eq. (3.4) at  $H = 250 \text{ nm}$  (lines) with the parameters summarized in Table 3-II. .... 28**

**Figure 3.4: HAADF image of InAs-InP nanowire from sample B1. .... 29**

<b>Figure 3.5: Length versus diameter for different Be doped InP nanowire segments grown on InAs bases (sample B1: undoped, sample B2: <math>4 \times 10^{19} \text{ cm}^{-3}</math>). Experimental data (symbols) are fitted by Eq. (3.4) at <math>H = 108 \text{ nm}</math> (lines) with the parameters summarized in Table 3-II. ....</b>	<b>30</b>
<b>Figure 4.1: Element count rate for the reference thin film InP standard. ....</b>	<b>41</b>
<b>Figure 4.2: Cross-sectional SEM images and corresponding SIMS data of counts per second as a function of depth for nanowire arrays a) A1, b) A4, c) A2, and d) A3. Scale bars in the SEM images represent <math>2 \mu\text{m}</math>. The values of <math>10^{-1}</math> are a proxy for ‘0’ on the log scale. ....</b>	<b>43</b>
<b>Figure 4.3: Carrier concentration as a function of depth for samples a) A2 and b) A3.....</b>	<b>46</b>
<b>Figure 5.1: Representative spectra from (a) sample A1, undoped, (b) sample A4, Be doping=<math>10^{17} \text{ cm}^{-3}</math>, (c) sample A2, Be doping=<math>10^{18} \text{ cm}^{-3}</math>, and (d) sample A3, Be doping=<math>2 \times 10^{19} \text{ cm}^{-3}</math>. Each spectrum is normalized to its dominant peak. ....</b>	<b>51</b>
<b>Figure 5.2: Distribution of the dominant peak energies emitted by the Be-doped InP nanowires (sample A1: undoped, sample A4: <math>10^{17} \text{ cm}^{-3}</math>, sample A2: <math>10^{18} \text{ cm}^{-3}</math>, sample A3: <math>2 \times 10^{19} \text{ cm}^{-3}</math>). ....</b>	<b>52</b>
<b>Figure 6.1: Tilted views (<math>45^\circ</math>) of InP nanowires doped with a) silicon and b) tellurium.....</b>	<b>60</b>

## LIST OF TABLES

<b>Table 3-I: Description of samples .....</b>	<b>24</b>
<b>Table 3-II: Fitting parameters .....</b>	<b>36</b>
<b>Table 4-I: Nanowire growth conditions .....</b>	<b>39</b>
<b>Table 4-II: InP material parameters .....</b>	<b>41</b>
<b>Table 4-III: Count rates near substrate .....</b>	<b>44</b>
<b>Table 4-IV: Nominal and measured carrier concentrations near substrate .</b>	<b>44</b>
<b>Table 5-I: Nanowire growth conditions .....</b>	<b>50</b>
<b>Table 5-II: InP material parameters for BGN calculation [51].....</b>	<b>55</b>

## LIST OF ABBREVIATIONS

1D	One-dimensional	HF	Hydrofluoric
2D	Two-dimensional	HRTEM	High-resolution scanning transmission electron microscope/microscopy
BF	Bright field	ICP	Inductively coupled plasma
BGN	Bandgap narrowing	MBE	Molecular beam epitaxy
CBE	Chemical beam epitaxy	MOVPE	Metalorganic vapour phase epitaxy
CCD	Charge-coupled device	PL	Photoluminescence
CCEM	Canadian Centre for Electron Microscopy	RSF	Relative sensitivity factor
CEDT	Centre for Emerging Device Technologies	SAD	Selected area diffraction
CVD	Chemical vapour deposition	SEM	Scanning electron microscope/microscopy
DI	Deionized	SIMS	Secondary ion mass spectrometry
DF	Dark field	TEM	Transmission electron microscope/microscopy
DP	Diffraction pattern	UHV	Ultra-high vacuum
EDS	Energy dispersive X-ray spectroscopy	UV	Ultra-violet
EHP	Electron-hole pair	VLS	Vapour-liquid-solid
FEG	Field emission gun	$\mu$ PL	Micro-photoluminescence
GS-MBE	Gas-source molecular beam epitaxy		
GT	Gibbs-Thomson		

## **Declaration of Academic Achievement**

The research presented in this thesis was performed by the author, with special assistance noted in the acknowledgments. The main body of Chapter 3 has been reprinted with permission from AIP Publishing LLC:

R.J. Yee, S.J. Gibson, V.G. Dubrovskii, and R.R. LaPierre, Applied Physics Letters **101**, 263106 (2012).

Other authors were:

**S.J. Gibson**, who provided valuable insight into the nucleation-limited growth regime;

**V.G. Dubrovskii**, who developed the model of nanowire growth based on the data and regime interpretation; and

**R.R. LaPierre**, who supervised the work and shared valuable expertise.

# Chapter 1

## Introduction

Over the last 50 years, humanity's desire for knowledge has driven rapid and innovative advances in computer technology. Moore's Law, originally an observation on the pace of transistor development from 1959 to 1965 [1], has become an ongoing, self-set challenge that semiconductor manufacturers strive to maintain. It has spurred research into novel materials and devices, particularly at the micro- and nano-scale first articulated by Feynman [2]. Nanowire technology is one such emergent field, fabricating and processing rod-like structures with monocrystalline lattices and very high length to diameter ratios.

The ability to produce ensembles of such small dimensions is more than an impressive technological feat, though; the geometry of nanowires enables engineers to take advantage of quantum confinement effects unique to 1D structures. These behaviours open the door to exciting research with wide-ranging applications in energy, computing, and lighting.

This introductory chapter will discuss the vapour-liquid-solid (VLS) theory of bottom-up nanowire growth, including important contributions to its development and understanding, as well as features specific to III-V epitaxial growth. The motivation for nanowire research, and the need for further study of

the effects of doping on growth will also be presented. Finally, the thesis organisation will be provided for the reader.

## 1.1 VLS Nanowire Growth

The most commonly accepted model for nanowire growth, vapour-liquid-solid theory, was first proposed by Wagner and Ellis in 1964 [3]. Their silicon “nanowhiskers” were free of the axial screw dislocations assumed necessary at the time for preferential 1D growth, known as the Frank mechanism [4]. Observing the absence of such dislocations in their nanowhiskers as well as the presence of globe-like particles at the tips, they suggested that a metal impurity, like gold, could act as a seed for nanowire growth. By growing at a temperature such that the impurity liquefied and formed droplets, the vapour-phase precursor species decomposed on the surface and alloyed with the gold particle. Wagner and Ellis hypothesized that the gold alloy would supersaturate, and the silicon would crystallize on the solid-liquid interface below. Thus the nanowire growth species would pass from a vapour precursor phase, to a liquid alloy, to a solid crystal. This process is illustrated in Figure 1.1.

It is notable that by 1975 VLS was commonly referenced in nanowire research papers, and at this time the theory was further refined by Givargizov to account for diameter dependences of the growth rate [5]. Polynuclear growth, determination of nucleation as the rate-limiting step, and the Gibbs-Thomson (GT) effect were all important considerations, but this last factor was the most

significant contribution. The GT effect describes the increase in vapour pressure and resultant decrease in solubility as the diameter of a particle decreases:

$$\Delta\mu = \Delta\mu_0 - \frac{4\Omega\alpha}{D} \tag{1.1}$$

where  $\Delta\mu$  is the difference in chemical potential between the growth species in the vapour and the droplet phases, and  $\Delta\mu_0$  is the difference in chemical potential between the growth species in the vapour and planar forms.  $\Omega$  is the atomic volume of the growth species;  $\alpha$  is the surface energy of the nanowire; and  $D$  is the diameter. Thus, for a diameter sufficiently small, a rounded particle is energetically disadvantaged and will deplete. This results in a ‘critical diameter’, usually 5 nm or smaller [6], below which nanowire growth is not observed.

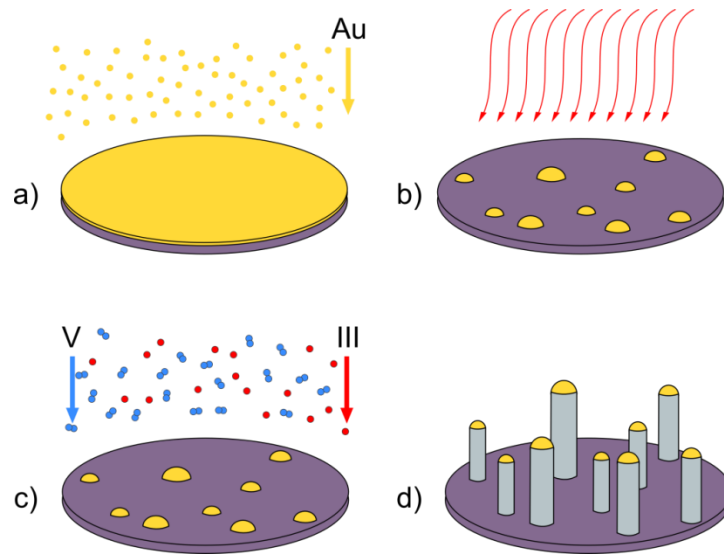


Figure 1.1: The VLS process. a) A catalyst material (i.e. gold) is deposited onto the growth substrate. b) The substrate is heated and the gold assembles into nanoparticles. c) Growth species (here, III-V elements) are introduced in vapour phase and alloy with the liquid droplets. d) Once the alloyed droplet has supersaturated, the growth material precipitates at the solid-liquid interface.

This updated model accounting for the GT effect was developed from chemical vapour deposition (CVD) experiments, and predicted a positive dependence of growth rate on diameter (i.e. nanowires with larger diameters grow to larger heights). However, studies of molecular beam epitaxy (MBE), chemical beam epitaxy (CBE), and metalorganic vapour phase epitaxy (MOVPE) growths did not display this trend; instead, an inverse relationship was observed. Johansson explained the phenomenon through a mass transport argument, showing the limiting factor to be not nucleation, but the collection area within which adatoms would be able to diffuse to the droplet-nanowire interface and incorporate [7]. The epitaxial experiments had a longer diffusion length compared to the species in CVD systems, and accordingly the adatom diffusion from the substrate and sidewalls had a more significant influence (Figure 1.2).

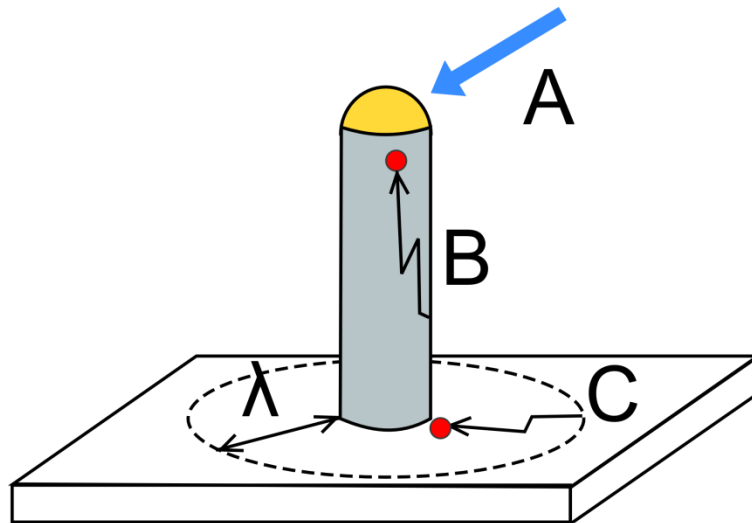


Figure 1.2: In addition to (A) direct impingement on the droplet, systems with non-negligible diffusion lengths ( $\lambda$ ) must account for diffusion from (B) sidewalls and (C) the substrate collection area.

Soon afterwards, the understanding of III-V semiconductor nanowire growth was expanded by the proposal of nucleation at the triple phase interface of the droplet, wire, and vapour. Through energy considerations, Glas et al argued that the introduction of a nucleus' solid-vapour interface at the edge of a nanowire top facet was the preferable position at high supersaturation. This also explained the wurtzite crystal structure and stacking faults frequently observed in III-V nanowires, in contrast with their zincblende bulk form counterparts [8].

Beyond these seminal contributions to the understanding of nanowire growth, many researchers have developed general models for different regimes and mechanisms of growth. These have included the onset of radial growth when the nanowire height exceeds the sidewall diffusion length [9, 10]; barrel shapes resulting from shadowing of the bases [11]; poly- and mono-nucleation of layers [12]; and the effect of sidewall wetting by droplets on the crystal structure [13].

Notably, Dubrovskii has developed a generalized nanowire growth model that accounts for both adatom diffusion as well as the GT effect, in both CVD and high vacuum epitaxy growth (MBE, CBE) [6]. This model describes two general diameter-dependent regimes of growth: one dominated by the GT effect where the higher solubility of large particles results in faster growth, and a second that is limited by mass transport considerations. Thus the transition from the first to the second results in a rapid increase in growth rate with diameter, followed by the inverse relationship characteristic of epitaxial systems.

Many effects of different growth conditions are still being examined, but two excellent reviews of progress to date can be found in references [14] and [15].

## **1.2 Motivations for Present Work**

Nanowires are interesting for the development of optoelectronic applications including light-emitting diodes [16], transistors [17], high-efficiency solar cells [18, 19], and sensors [20, 21]. The distinct nanostructure has many benefits for bandgap energy tuning of photodetectors and enhanced light trapping in solar cells. Additionally, nanowires are able to relax significantly more strain across abrupt compositional interfaces than their planar equivalents [22]. This flexibility of lattice mismatch widens the range of materials that can be used in axial (segmented) and radial (core-shell) heterostructure devices.

However, with increased interactions in materials systems it becomes much more challenging to control and predict the growth and characteristic features of the final ensemble. Dopant incorporation, for example, is essential for the fabrication of optoelectronic devices, particularly in the formation of p-n junctions. However, although it is a well understood area of thin film engineering, there is still much unknown about the effects of doping on nanowire growth. Doping studies have shown changes in crystal structure and periodic polytypism [23, 24]; kinking and crawling growth [25, 26]; axial growth rate [24, 25, 27]; and radial growth rate [18, 28]. The geometry also requires consideration of radial doping uniformity and depletion [29]. These effects are not necessarily

detrimental to nanowire growth, but do represent real challenges to predictable and well-understood device design.

Thus, the research presented here was motivated by the desire to understand the effects of doping in InP nanowire ensembles, which are of special interest for high-efficiency devices due to their high carrier mobilities. The use of a MBE system for such a doping study is ideal because it eliminates the higher number of interactions present in metalorganic systems.

### **1.3 Thesis Overview**

This thesis will present the characterization of an InP nanowire doping study. Ensemble samples were prepared with varying levels of Be doping, permitting a systematic examination of the effects of doping on the growth rate, composition, and bandgap transitions.

Chapter 2 will discuss the sample preparation method, including the basic mechanics of the molecular beam epitaxy (MBE) system used for nanowire growth. Characterization techniques will also be detailed for scanning and transmission electron microscopy (SEM and TEM); compositional analysis through secondary ion mass spectrometry (SIMS); and optical studies with micro-photoluminescence ( $\mu$ PL). Chapter 3 is the most significant part of the thesis, describing a transition in nanowire growth regimes with increased Be doping of InP nanowires. The effects on growth rate, heterostructure form, and crystal

structure were investigated through SEM and TEM study. A model of the growth rate as a function of diameter developed in collaboration with V. G. Dubrovskii is also presented. This chapter is a minimally revised version of an article previously published in *Applied Physics Letters* [30], and hypothesizes a change from a diffusion-limited regime to a nucleation-limited regime with increased doping. Further characterization of the doping study is discussed in Chapter 4 and Chapter 5, examining the dopant incorporation through SIMS analysis and the dopant activation through  $\mu$ PL experiments, respectively. Finally, conclusions and avenues for future work are presented in Chapter 6.

## **Chapter 2**

### **Growth and Characterization Techniques**

This chapter will introduce the growth process of the nanowires studied in this work, and describe the methods used to characterize them. The molecular beam epitaxy system and the preparation of wafers for sample growth will be outlined. Characterization methods include scanning and transmission electron microscopy, secondary ion mass spectrometry, photoluminescence, and the preparation of samples for each technique.

#### **2.1 Molecular Beam Epitaxy**

Epitaxy is the growth of a material that takes the same crystal structure as the substrate or film it rests upon. Molecular beam epitaxy (MBE) systems, originally developed in the early 1970s for the telecommunications industry, are capable of producing single crystal thin films. The ultra-high vacuum (UHV) environment in the deposition chamber permits molecular flow that is controlled by shutters, enabling epitaxial growth and precise control of the layer structure. MBE does not scale well to large production, and thus is typically used for research purposes or specialized devices that require high quality performance.

The gas-source molecular beam epitaxy (GS-MBE) system operated by the Centre for Emerging Device Technologies (CEDT) at McMaster University

has a mixture of solid and gas sources to produce a variety of III-V structures. Indium, gallium, aluminium, antimony, silicon, beryllium, and tellurium sources are housed in individual effusion cells which can heat to  $\sim 1000^{\circ}\text{C}$ , vaporizing the elements. When the shutter is opened, the high vacuum of the deposition chamber and the vapour pressure of the effusion cells form a diffusion gradient that drives the molecular flow from the cell to the substrate. As the source is depleted over time or replaced, growth temperatures must be re-calibrated to properly control the vapour pressure and flow.

Hydride forms of arsenic (arsine,  $\text{AsH}_3$ ) and phosphorus (phosphine,  $\text{PH}_3$ ) are used instead of solid sources to avoid the high vapour pressures that result in rapid depletion for these elements. They are introduced to the deposition chamber by valved crackers that decompose the molecules into the dimer forms  $\text{As}_2$  and  $\text{P}_2$  (which additionally have higher sticking coefficients than the tetramers from solid sources). Due to the toxic nature of the gases, the feed to the cracker is shielded and a scrubber used to clean the elements pumped from the chamber.

To maintain ultra-high vacuum conditions on the order of  $10^{-9}$  Torr in the deposition chamber, a separate chamber is used to load the samples. Evacuation of this load lock before transferring the sample to the deposition chamber minimizes contamination from atmospheric conditions. To maintain vacuum conditions during growth, a turbo pump backed by a roughing pump is used, aided by a cryogenic pump that cools the walls with liquid nitrogen. Thus, molecules

and contaminants are primarily removed by the turbo pump mechanically, and the excess are adsorbed onto the wall surfaces. Figure 2.1 shows a schematic of the CEDT GS-MBE system.

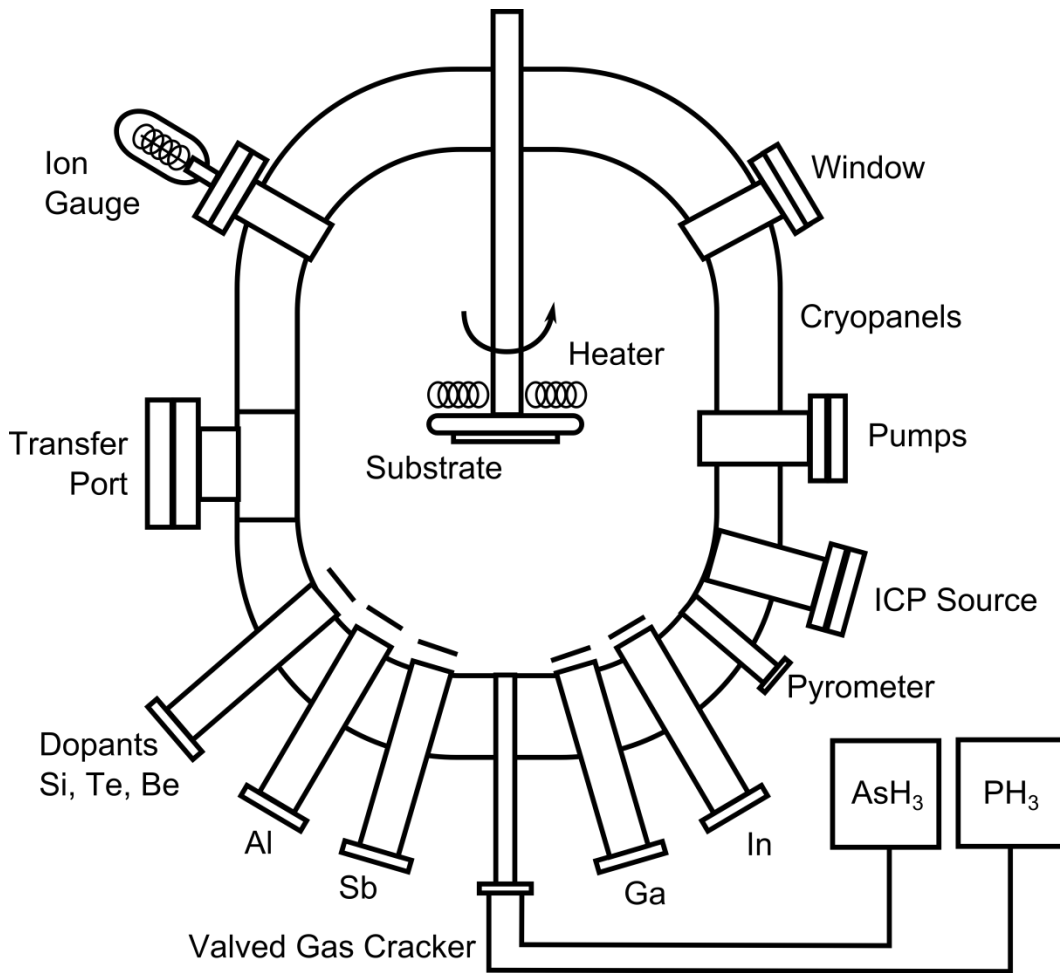


Figure 2.1: Diagram of the GS-MBE deposition chamber operated by the CEDT. Image used with permission from [31].

## 2.2 Sample Preparation

All samples were grown on single side-polished, 3" nominally undoped (n-type,  $(1-10) \times 10^{15} \text{ cm}^{-3}$ ) InP (111)B wafers manufactured by AXT, Inc. In preparation for cleaning and a gold thin film deposition, wafers were removed from their packaging in a cleanroom and cleaned by UV ozone oxidation for 20 minutes. They were subsequently cleaned by a 10% buffered hydrofluoric (HF) acid etch for 30 seconds, then rinsed under flowing deionized (DI) water for 10 minutes. Wafers were dried with nitrogen and loaded into an electron beam evaporator. After evacuating the chamber to a deposition pressure of  $10^{-8}$  Torr, 1 nm of Au was deposited at a rate of 0.1 nm/s using a quartz crystal detector for calibration.

Prior to growth, wafers were cleaved into 6 equal wedges for economy and consistency among growths. A diamond scribe was used to repeatedly nick the midpoint of the secondary flat. Next, positioning the wafer polished side down in a concave wafer holder and applying a gentle pressure to the marked edge propagated the cleave across the wafer. The process was then repeated, using a cutout metal stencil of a  $60^\circ$  angle to mark the segment edges and cleave each wafer halves into three equal pieces.

Once loaded into the MBE system, each segment underwent a degas procedure for 15 minutes at  $250^\circ\text{C}$  and oxide desorption at  $475^\circ\text{C}$ . Following this,

the growth parameters were specific to the samples, and will be described in later chapters.

### 2.3 Electron Microscopy

Electron microscopy was first proposed in the early 1930s as a method of overcoming the resolution limits of visible-light microscopes. The Rayleigh criterion describes the smallest resolvable distance in an image as:

$$\delta = \frac{0.61\lambda}{\mu \sin \beta} \quad (2.1)$$

where  $\mu$  is the refractive index between the lens and the nanowire, and  $\beta$  is the semi-angle of the magnifying lens. It is clear that a higher resolution requires a shorter wavelength, which is related inversely to an increase in the electron's speed by Eq. (2.2):

$$\lambda = \frac{h}{p} = \frac{h}{mv} \quad (2.2)$$

where Planck's constant  $h = 6.626 \times 10^{-34}$  J s and  $p$  is momentum, the product of the electron's mass ( $m = 9.1 \times 10^{-31}$  kg) and speed.

By moving an electron through an accelerating voltage  $V$ , it gains a potential energy  $eV$ . As this is transformed to kinetic energy, the electron's speed increases in proportion to the square root of the accelerating voltage:

$$eV = \frac{m_0 v^2}{2} \Rightarrow v = \sqrt{\frac{2eV}{m_0}} \quad (2.3)$$

Relating Eq. (2.3) to Eq. (2.2), Eq. (2.4) shows the inverse relationship between wavelength and accelerating voltage:

$$\lambda = \frac{h}{p} = \frac{h}{m\sqrt{2eV/m_0}} = \frac{h}{\sqrt{2m_0eV}} \quad (2.4)$$

Finally, accounting for relativistic effects the dependence of wavelength on the accelerating voltage is more accurately described by:

$$\lambda = \frac{h}{\sqrt{2m_0eV(1 + eV/2m_0c^2)}} \quad (2.5)$$

for  $c = 3 \times 10^8$  m/s. Using a typical TEM accelerating voltage of 120 kV thus results in a (theoretical) resolution limit of approximately 4 pm. At this scale, features such as stacking faults, crystal lattice structure and compositional contrast can be resolved with appropriate alignment and image correction.

For the work presented in this thesis, scanning and transmission electron microscopy work was completed at the Canadian Centre for Electron Microscopy, located at McMaster University.

### 2.3.1 Scanning Electron Microscopy

To observe the morphological features of nanowire arrays, a scanning electron microscope (SEM) was used to study their dimensions, directionalities,

and densities. SEM images are formed by scanning an electron beam across the sample, causing the ejection of conduction band electrons called secondary electrons. These energized secondary electrons are ejected from the sample and collected by a detector, which correlates the intensity of signal with the scanning position to produce an image. The technique is surface-sensitive due to the small escape depth of the low energy secondary electrons.

SEM specimens were prepared by affixing small pieces (minimum area of  $5 \text{ mm}^2$ ) cleaved from nanowire arrays to metal stubs. Debris was minimized by partially scribing cleave lines parallel to the edges, and propagating the cleave from the marked edges to protect the interior. The specimen was then mounted on a  $45^\circ$  angled stub with carbon tape, and silver paste applied from the edges to the stub to improve grounding between surfaces and minimize charging from the electron beam. Use of a  $45^\circ$  stub allowed the arrays to be studied from 3 key angles to the nanowire axes:  $90^\circ$  (profile view),  $45^\circ$ , and  $0^\circ$  (plan view).

The stub was then loaded in the loading chamber of the JEOL JSM 7000F, which was evacuated before transferring the sample holder to the stage in the primary chamber. The system was pumped down to a pressure of  $5 \times 10^{-5}$  Torr before switching on the Schottky field emission gun (FEG) used to generate the scanning ion beam. Gun voltage was set to 15 eV, and lowered down to 5 eV to avoid charging issues for samples with poor grounding or an insulating cyclotene layer. The focal length was set between 5 and 10 mm, and the image scale automatically generated by the SEM software.

### 2.3.2 Transmission Electron Microscopy

To probe beyond the surface of the nanowires, a transmission electron microscope (TEM) was used to reveal details of the nanowire crystal structure, consistency, and composition. When first developed, TEM specimens were often metallic but today encompass a wide variety of materials and structures that can be prepared by different thinning, separation, and etching techniques. To prepare nanowire specimens for analysis, small pieces were cleaved from the sample as previously described for SEM (Section 2.3.1). However, for TEM analysis the samples must be thin enough to be transparent to the electron beam; thus, the nanowires were separated from the substrate by sonicating the cleaved piece in approximately 10 mL of methanol for 30 seconds. The suspended nanowires were then transferred via micropipette to a holey carbon grid and the methanol evaporated in ambient air leaving the nanowires on the grid. The transfer and evaporation process was repeated for a total of 8-15 $\mu$ L until an appropriate density was achieved.

For straightforward measurements of dimensions and crystal structure, the Philips CM12 TEM was used in bright field (BF) and diffraction pattern (DP) modes, respectively. In BF images, the intermediate lens is focussed so the image plane of the objective lens is the object plane magnified throughout the system. A charge-coupled device (CCD) camera positioned below the fluorescent display screen can be used to record images and calibrate the scale of magnification. In DP analysis, the nanowire is tilted along and about its axis until it is aligned to the

electron beam, and a selected area diffraction (SAD) aperture used to exclude the electron beam from regions outside the area of interest. The diffraction of the electron beam through the crystal lattice projects a pattern of bright spots and forbidden reflections unique to specific lattice planes. Since the intensity of the bright spots is too high for the CCD camera to process, photographic emulsion plates are used to record the patterns, and scanned after processing. However, while aligning for SAD, the  $[01\bar{1}0]$  wurtzite plane must be avoided as stacking faults are not visible along this plane; additionally, the diffraction pattern is difficult to distinguish from the  $[1\bar{1}\bar{2}]$  plane of zinc blende. Thus in this work, the  $[2\bar{1}\bar{1}0]$  wurtzite plane was used for all alignments.

The JEOL 2010F high resolution scanning transmission electron microscope (HRTEM) was used for more detailed verification of compositional structure using high-angle annular dark field (HAADF) imaging and energy dispersive X-ray spectroscopy (EDS, also referred to as EDX or XEDS). HAADF images were obtained by detecting electrons scattered forward through the specimen at higher angles than those detected in BF and DF images. The increase in scattering angle for larger  $Z$ -numbers results in image intensity variation and provides a visual indication of compositional changes. This was used to aid understanding of heterostructure growth, described further in Section 3.3. EDS is a technique that identifies the compositional elements of a specimen. If the electron beam is sufficiently energetic, core electrons from the inner shell are ejected to a higher energy level. When another electron in the shell structure fills

the empty lower state, the energy loss is radiated as a characteristic X-ray that can be referenced to identify the element. The probability of X-ray generation in EDS increases with Z-number, and so is a poor choice for identifying light elements. Thus, another technique, secondary ion mass spectrometry, was used for detection of beryllium dopants in the nanowires.

## **2.4 Secondary Ion Mass Spectrometry**

Dynamic secondary ion mass spectrometry (SIMS) is a technique used to analyze the compositional depth profile of a bulk material. By rastering an ion beam across the analytical area, elements are sputtered and identified by mass spectrometry (also referred to as mass spectroscopy). As atoms are sputtered, the ion beam targets progressively deeper areas of the sample, and a profile of the element counts at each level is developed.

For thin films with uniform height, no special sample preparation is necessary. Nanowire arrays, however, provide a challenge to SIMS because of the ion beam's simultaneous access to the nanowire layers (which may have an uneven height profile) as well as the substrate. To enable a uniform rate of sputtering across the array, nanowire samples must be spin-coated with cyclotene to fill the voids between nanowires and transform the array into a "bulk-like" material. For the samples presented in this thesis, approximately 3 mL of cyclotene was deposited onto the nanowire arrays. After resting for 5 minutes to let the cyclotene sink between the nanowires, the sample was placed on a

spincoater. The spin speed was ramped from 0 – 5000 RPM in 17 seconds, and held at the maximum speed for 1 minute. Following this, the samples underwent a soft bake at 100°C for 90 seconds, and a hard bake at 250°C for 30 minutes, after a temperature ramp of 5°C/minute. The cyclotene is sputtered at the same rate as the nanowires, and further information detailing this technique can be found in reference [32].

The SIMS analysis presented in this thesis was performed at Surface Science Western at the University of Western Ontario. The system uses a Cameca IMS-6f ion microprobe to raster an area of 250 $\mu\text{m}$  x 250 $\mu\text{m}$ , and analyzes a circular area 60 microns in diameter in the centre of the crater. When selecting the ion beam for analysis, relative sensitivity factors (RSFs) must be considered for greatest sensitivity to the elements of interest, especially those only present in small quantities. Here, an oxygen beam was used to maximize sensitivity to the beryllium dopants. The results obtained are discussed in Chapter 4.

## **2.5 Micro-Photoluminescence Spectroscopy**

Photoluminescence (PL) studies are used to characterize the electronic band structure of semiconductors. In a micro-photoluminescence ( $\mu\text{PL}$ ) system, the laser can be positioned to focus on a single nanowire, which can later be located in SEM to match the electronic properties with the morphological features. Specimens for PL were prepared similarly to those for TEM (Section 2.3.2). For photoluminescence, a holey carbon grid was incapable of sufficiently

dissipating the energy of the laser's power, and a silicon chip used as the substrate instead. To prepare the silicon chip for use, it was lightly marked using a diamond tip scribe to aid comparison between visual-light microscope images and the PL system's monitor display of the surface. The silicon chip was then sonicated in methanol to clean it of debris, and a suspended nanowire solution transferred by micropipette and evaporated.

To optically characterize the nanowires, a laser is used to excite the electrons and generate electron-hole pairs (EHPs). Upon their recombination, photons are radiated with wavelengths indicative of the energy gap between the conduction and valence bands (although complex transitions between other levels may also appear). With increased impurity doping, a secondary peak related to the impurity transitions appears at a higher wavelength, and rises in intensity relative to the primary bandgap energy with increased carrier concentration. Eventually, the secondary peak may overwhelm the initial bandgap transition.

Micro-PL studies were completed at McMaster University (layout shown in Figure 2.2), using the components described below. The results of the  $\mu$ PL studies are discussed in Chapter 5.

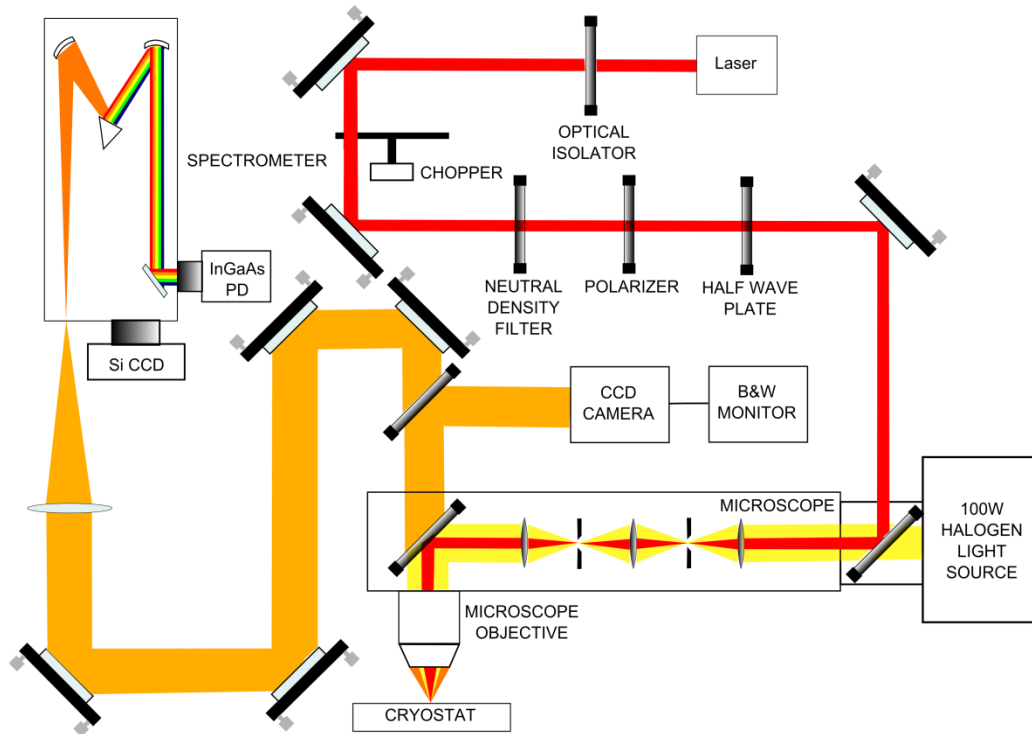


Figure 2.2: Layout of the micro-photoluminescence system used to optically characterize nanowires. Image used with permission from [31].

*Laser:* A Melles Griot 35LAP431-208 argon-ion laser was used for the PL studies, linearly polarized with an extinction ratio of 500:1. The wavelength was tuned to  $\lambda=488$  nm (energy  $E=2.54$  eV), with a power of  $P=130$  mW. The intensity could be modified by a selection of neutral density filters in a rotating wheel installed in the beam path, with optical densities between 0.1 and 4.

*Optical components:* The optics of the system included a polarizer, half wave plate, filters, silvered mirrors, and a beam splitter to modify and direct the path of the laser beam. A Glan-Thompson polarizer was used to polarize the light with a higher extinction ratio of 100000:1. The half-wave plate that followed was

used to rotate the polarization along the nanowire's length for optimized absorption and luminescence from the nanowire. Filters and mirrors were used to direct the path of the beam, and a beam splitter was used to divide the path between both the spectrometer and the CCD camera. The CCD camera connected with a monitor aided the positioning of the laser on the target nanowire.

*Spectrometer and Detector:* An asymmetric Czerny-Turner spectrometer (Horiba Jobin Yvon iHR550) was used to measure the spectral response of the sample. A Horiba Symphony II silicon CCD detector measured the spectrometer output over a range of 350-950nm, and was cooled by liquid nitrogen to minimize dark current. The chip had a back-illuminated design, a resolution of 1024x128 pixels, and was also produced by Horiba Jobin Yvon.

*Cryostat:* A Janis ST-500 constant gas flow helium cryostat was used to cool the sample during experiments, minimizing the lattice vibrations that reduce radiative recombination (and therefore luminescence) of EHPs. The sample was held in a contained area evacuated to  $10^{-4}$  Torr before flowing liquid helium through tubing around the sample stage.

## Chapter 3

### Effects of Be-Doping on InP Nanowire Growth

#### 3.1 Introduction

In this chapter, the effect of Be doping on MBE-grown InP nanowire growth is examined, where a suppression of growth rates with increasing dopant concentration is shown for small diameter nanowires. It is speculated that Be at high dopant concentrations may increase the steady-state chemical potential of the Au-InP catalyst droplet, leading to the corresponding decrease of liquid and adatom supersaturation during growth. This causes a transition from the typical inverse growth rate dependence on diameter to an increasing one where for small nanowire diameters the axial growth rate is suppressed. These observations provide a different perspective on the effects of doping on nanowire growth, and were reported by the author of this thesis (R.J. Yee), S.J. Gibson, V.G. Dubrovskii, and R.R. LaPierre in *Applied Physics Letters* [30].

Note that although the article discussed three InP nanowire samples A1, A2, and A3 (undoped, and Be-doped at levels of  $1 \times 10^{18} \text{ cm}^{-3}$  and  $2 \times 10^{19} \text{ cm}^{-3}$ ), a fourth InP nanowire sample Be-doped at  $1 \times 10^{17} \text{ cm}^{-3}$  was also characterized. Its properties were consistent with the rest of the study, but the effect on the growth rate at this low doping level was slight, and overlapped with the undoped sample. Thus for clarity it was not included in the published article.

### 3.2 Experimental Details

InP (111)B wafers were cleaned by UV ozone oxidation for 20 minutes followed by buffered HF etching for 30 seconds. This was followed by e-beam evaporation of 1 nm of Au. Wafers were then cleaved into 6 segments for separate growths as outlined in Table 3-I. Nanowires were grown by gas source molecular beam epitaxy (GS-MBE) using an In effusion cell and group V dimers ( $\text{As}_2$ ,  $\text{P}_2$ ) derived from a hydride gas cracker. All samples underwent a degas for 15 min at 250 °C and oxide desorption for 10 min at 475 °C. All nanowires were grown at 420°C with a 2-D equivalent growth rate (In impingement rate) of 0.5  $\mu\text{m}/\text{h}$ .

Table 3-I: Description of samples

<b>Sample</b>	<b>Structure (Growth Duration)</b>	<b>Nominal carrier concentration by Be doping (<math>\text{cm}^{-3}</math>)</b>
A1	InP (30 min)	undoped
A2	InP (30 min)	$10^{18}$
A3	InP (30 min)	$2 \times 10^{19}$
B1	InAs (30 min) / InP (13 min)	undoped
B2	InAs (30 min) / InP (13 min)	$4 \times 10^{19}$

Samples A1-A3 consisted of InP nanowires with increasing Be dopant concentration, provided by a Be effusion cell. Nominal carrier concentrations

were based on Hall effect measurements on InP epilayers. Samples B1 and B2 were first comprised of a base InAs segment, followed by an InP segment. The V/III flux ratios were 5.6 and 3.6 for InP and InAs, respectively, in all samples.

Nanowire morphology was examined by scanning electron microscopy (SEM) using a JEOL 7000F. Nanowires were prepared for transmission electron microscopy (TEM) by sonicating a cleaved piece of sample in methanol and drop-casting the solution on a holey carbon grid. Nanowire crystal structure was examined by a Philips CM12 TEM. Samples B1-B2 were examined by high angle annular dark field (HAADF) in a JEOL 2010F TEM.

### **3.3 Results and Discussion**

SEM analysis of the InP nanowires from samples A1-A3, shown in Figure 3.1 a-c, respectively, indicated a rod morphology with no observable tapering. Hence, the nanowire diameter was approximately equal to the Au droplet diameter. The nanowires grew vertical to the (111)B surface of the substrate with lengths up to 1.8  $\mu\text{m}$ , and diameters ranging from 20 nm to 140 nm corresponding to the initial size distribution of the Au droplets. The size distribution of Au droplets at the end of the nanowires after growth was identical among samples A1-A3. Thus, Be doping had no effect on the Au particle size distribution.

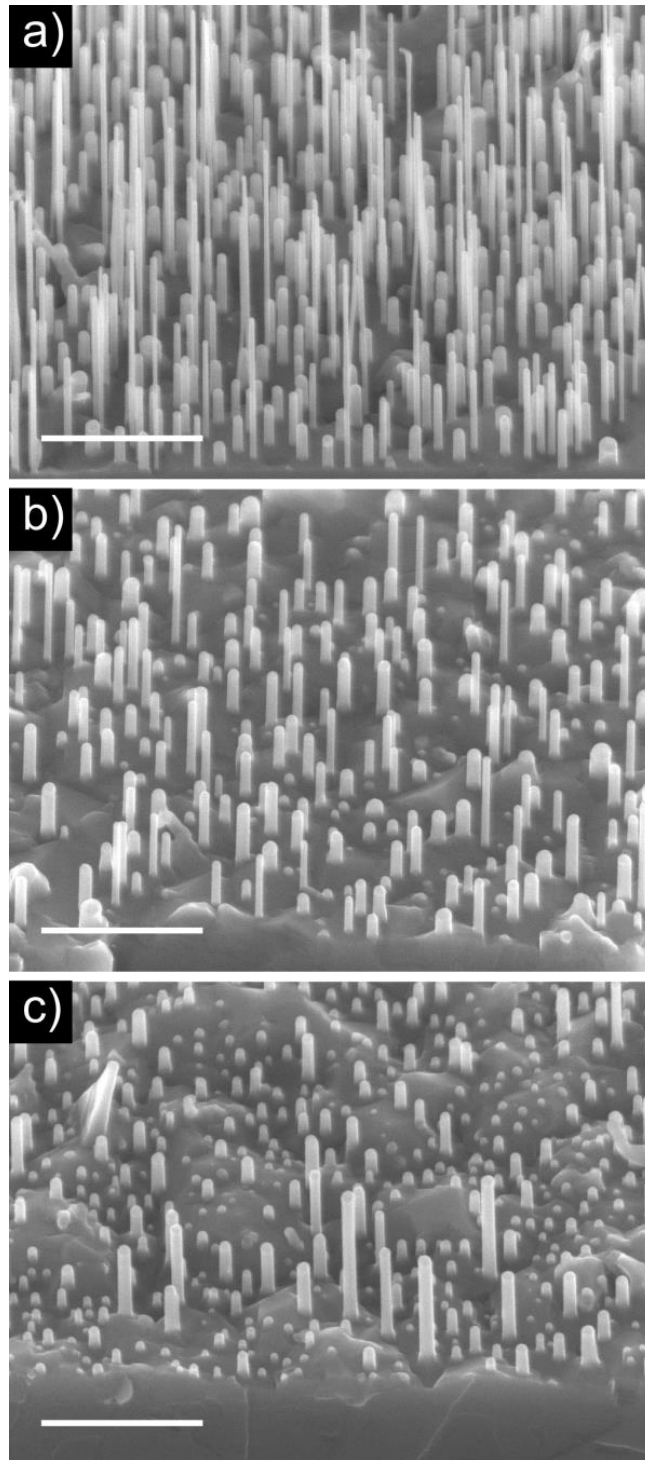


Figure 3.1: Tilted view ( $45^\circ$ ) SEM images of (a) sample A1, undoped, (b) sample A2, Be doping =  $10^{18} \text{ cm}^{-3}$ , and (c) sample A3, Be doping =  $2 \times 10^{19} \text{ cm}^{-3}$ . Scale bars indicate 1  $\mu\text{m}$ .

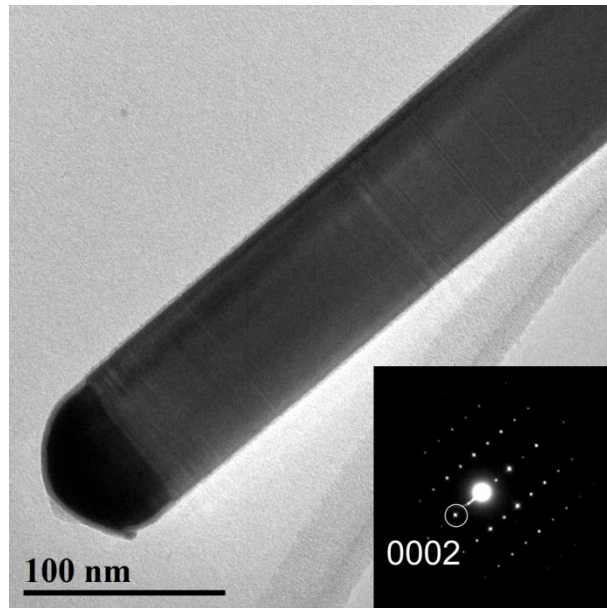


Figure 3.2: TEM image of typical nanowire from sample A3. Inset shows SAD pattern indicating the wurtzite crystal structure.

TEM analysis in Figure 3.2, and a corresponding selective area diffraction pattern given in the inset, indicated a wurtzite crystal structure for all samples A1-A3 with the nanowire axis oriented along the (0001) growth direction, as commonly observed in nanowires [33]. The Au droplet is also visible at the tip of the nanowire (bottom left of Figure 3.2). Stacking faults, also commonly observed in nanowires [34], appeared as contrast stripes across the nanowires as in Figure 3.2. Stacking faults were present in all samples A1-A3 with an increased occurrence in smaller diameter nanowires ( $\sim 0.2$  faults/nm) compared to larger diameter nanowires ( $\sim 0.06$  faults/nm). However, Be doping concentration did not appear to have any influence on the stacking fault density or crystal structure.

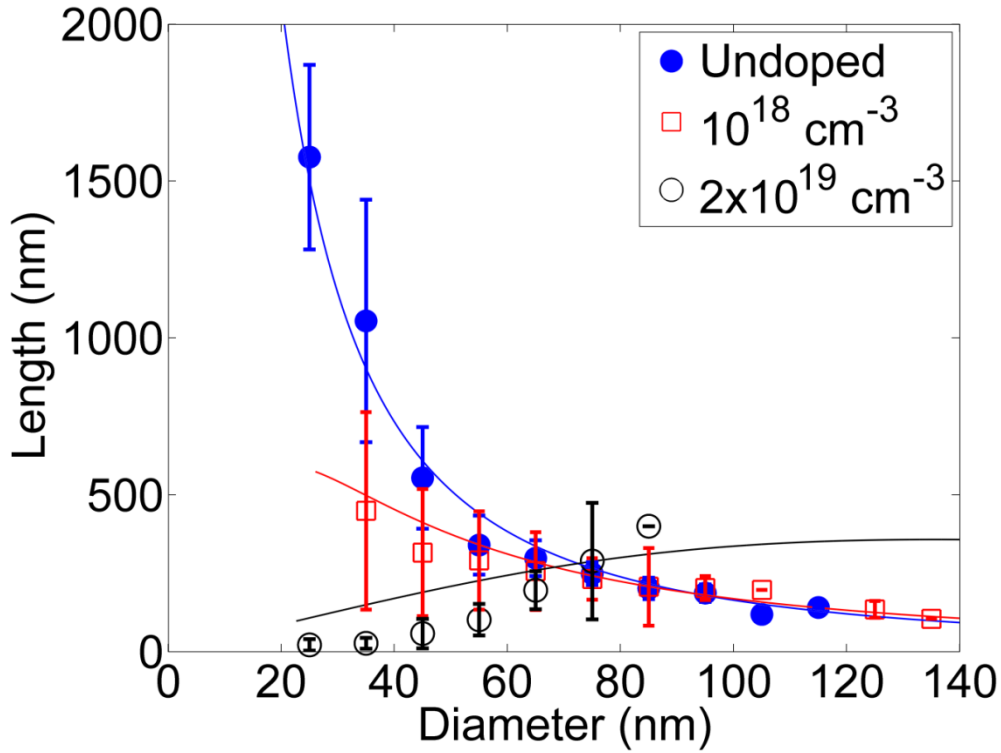


Figure 3.3: Length versus diameter for different Be doped InP nanowires (sample A1: undoped, sample A2:  $10^{18} \text{ cm}^{-3}$ , sample A3:  $2 \times 10^{19} \text{ cm}^{-3}$ ). Experimental data (symbols) are fitted by Eq. (3.4) at  $H = 250 \text{ nm}$  (lines) with the parameters summarized in Table 3-II.

Next, the length versus diameter [ $L(D)$ ] dependence of the InP nanowires was examined. Due to the formation process of Au droplets, a wide dispersion in nanowire diameters was obtained, allowing a study of the  $L(D)$  dependence. The lengths and diameters of nanowires were obtained directly from SEM images. The lengths are plotted against nanowire diameters in Figure 3.3. Each symbol represents an average length measured from up to 35 nanowires within a 10 nm diameter range, and error bars show the standard deviation. As seen in Figure 3.3,

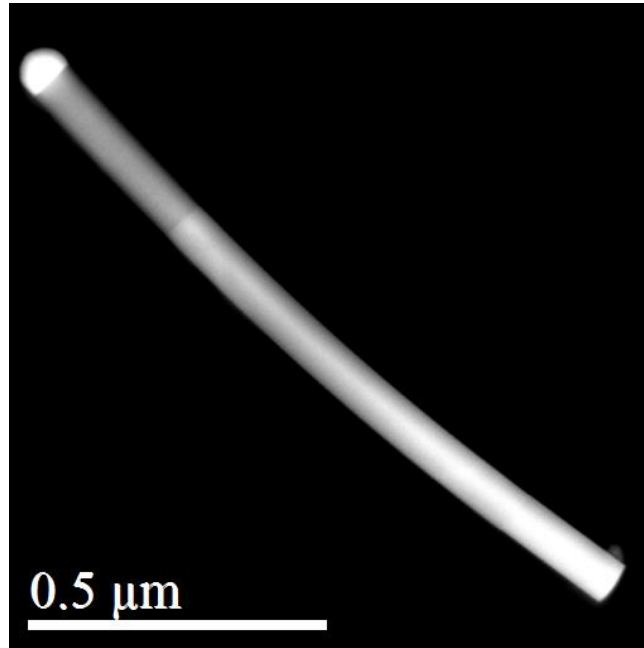


Figure 3.4: HAADF image of InAs-InP nanowire from sample B1.

for undoped nanowires the length shows an inverse relationship with diameter. This decreasing  $L(D)$  relationship indicates that growth is limited by adatom diffusion to the Au droplet from the nanowire sidewalls or surrounding substrate, as described previously [35]. However, as the Be concentration increased, a suppression of the growth rate occurred for nanowire diameters below  $\sim 70$  nm, resulting in an increasing  $L(D)$  relationship saturating at a length of about 400 nm for the doping level of  $2 \times 10^{19} \text{ cm}^{-3}$ .

To more thoroughly examine the mechanisms of the  $L(D)$  dependence shown in Figure 3.3, a similar study was performed using the InAs/InP heterostructure samples (B1 and B2). The contrast between the InP and InAs

segments in HAADF imaging (Figure 3.4) enabled the measurement of the top InP segment length, using the bottom InAs segment as a marker layer. Sample B1, which had a nominally undoped InP segment, featured the typical inverse  $L(D)$  relationship shown in Figure 3.5, similar to that of undoped InP nanowires. In comparison, sample B2 with a Be doping concentration of  $4 \times 10^{19} \text{ cm}^{-3}$  showed the unusual increasing  $L(D)$  relationship, also shown in Figure 3.5. Thus, samples B1 and B2 showed that the unusual  $L(D)$  behavior is not associated with differences in the initiation of growth, such as an incubation time.

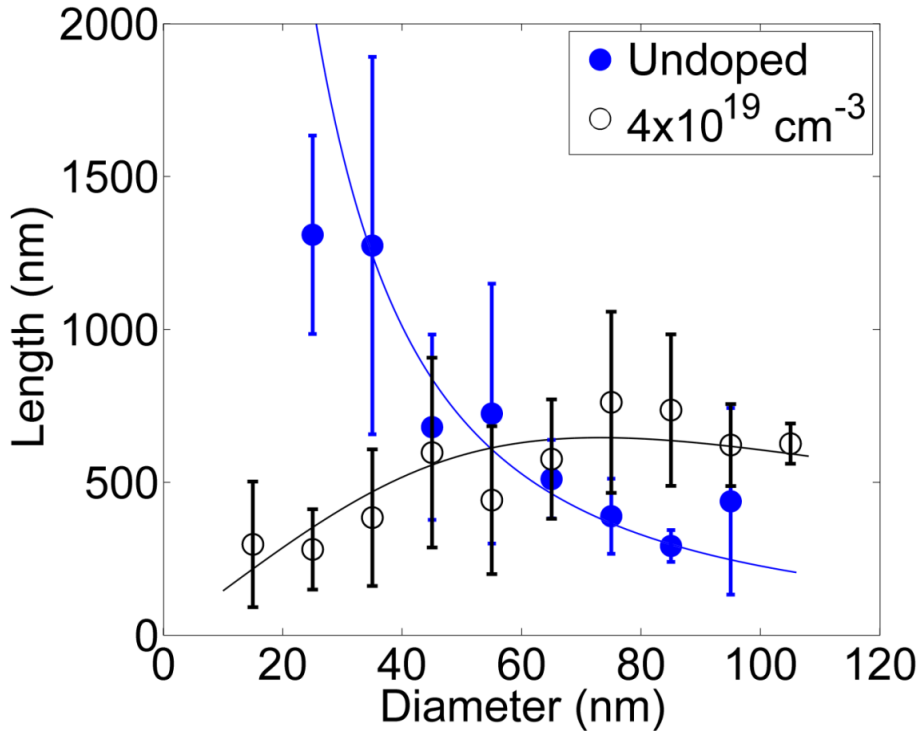


Figure 3.5: Length versus diameter for different Be doped InP nanowire segments grown on InAs bases (sample B1: undoped, sample B2:  $4 \times 10^{19} \text{ cm}^{-3}$ ). Experimental data (symbols) are fitted by Eq. (3.4) at  $H = 108 \text{ nm}$  (lines) with the parameters summarized in Table 3-II.

The reproduction of doping effects in the heterostructures also excluded a change in adatom diffusion as a cause of the  $L(D)$  behavior. Previous studies of Be-doped GaAs [26], Te-doped GaAs [18], Si-doped InAs [28], and Si-doped InP nanowires [27] indicated a reduction in length and an increase in tapering of the nanowires with doping. However, no  $L(D)$  relationships were presented directly in these previously published studies. These prior results suggested that dopants, present on the nanowire surface during growth, may influence diffusion length via surfactant effects or surface passivation, resulting in a preference for radial as compared to axial nanowire growth and a tapered nanowire morphology. However, such a tapered morphology was not observed in our A1-A3 nanowires. Furthermore, such a suppression of adatom diffusion length would be expected to produce a core-shell structure in our nanowire heterostructures, but this was not observed in samples B1 or B2. Instead, the TEM analysis of the InAs-InP nanowires in samples B1 and B2 indicated a purely axial growth, with no visible tapering or core-shell (radial) growth regardless of doping concentration. Previously, it was argued that InAs-InP heterostructures grown by GS-MBE are predominantly axial due to the long In adatom diffusion length that exceeds typical nanowire lengths as in the present results [36]. The axial nature of the heterostructures and absence of radial growth excludes a reduction in diffusion length as the cause of the unusual  $L(D)$  dependence in the InP nanowires.

### 3.4 Model of Length Dependence on Diameter

The  $L(D)$  relationship at low Be concentration is best fit by  $L \propto 1/D^2$ . This relationship is characteristic of diffusion-limited growth, and is derived from the relationship between adatom diffusion length and the In adatom collection area [37]. This inverse  $L(D)$  dependence is relevant when the In collection length on the substrate is much larger than the nanowire diameter, and the diffusion length on the nanowire sidewalls is much longer than the nanowire length. Since the lengths of our nanowires far exceed the deposition thickness of  $H = 250$  nm, the direct impingement on the droplet surface as well as the surface growth burying the nanowire root can be ignored. The growth rate in this case can thus be written in the form [11, 37]:

$$\frac{dL}{dt} = \left(\frac{2\lambda}{D}\right)^2 \left(\frac{\eta - \zeta}{\eta + 1}\right) V \quad (3.1)$$

where  $V$  is the deposition rate (nm/s),  $\lambda_s$  is the effective collection length of In,  $\zeta$  is the droplet supersaturation, and  $\eta$  is the adatom supersaturation with respect to the Au alloy droplet equilibrium (itself measured with respect to the solid wurtzite nanowire phase). Thus,  $\eta - \zeta$  is the adatom supersaturation with respect to a non-equilibrium droplet, and the resulting diffusion flux is directed to the droplet only when  $\eta > \zeta$ .

At  $\eta \cong \zeta$ , the diffusion transport into the droplet should equal the nanowire growth rate [12, 37]. For modest diameters, growth proceeds in the mononuclear regime where only one 2-D island emerges in each nanowire layer,

rapidly spreading to fill the complete monolayer [8, 38]. In such a regime, the growth rate is given by [37, 38]:

$$\frac{dL}{dt} = h\pi D r_c(\zeta) I(\zeta) \cong h\pi D r_c(\eta) I(\eta) \exp\left[-i_c(\eta) \left(\frac{\eta - \zeta}{\eta + 1}\right)\right] \quad (3.2)$$

where  $h$  is the height of a monolayer,  $I(\zeta)$  is the nucleation rate and  $r_c(\zeta)$  is the radius of the critical 2D nucleus. The nucleation rate  $I(\zeta)$  is approximated in the last expression on the right-hand side of Eq. (3.2) at  $\eta \cong \zeta$ , due to an extremely steep exponential dependence on the supersaturation [12]. The quantity  $i_c(\eta) \gg 1$  is the number of In atoms forming the critical island nucleus for  $\zeta = \eta$ . Note that our InP nanowires have a wurtzite crystal structure; thus, Eqs. (3.1) and (3.2) should use the wurtzite phase equilibrium values for the chemical potential. Furthermore, since only nucleation on the triple phase line favors the formation of wurtzite [8] the available nucleation area in Eq. (3.2) should be restricted to  $\pi D r_c$  rather than the full top facet  $(\pi D^2)/4$  [38].

Relating Eqs. (3.1) and (3.2), we obtain:

$$x e^x = \left(\frac{D}{D_0}\right)^3 \quad (3.3)$$

where  $x = i_c(\eta)(\eta - \zeta)/(\eta + 1)$ , and  $D_0 = \left[(4V\lambda_s^2)/(\pi h i_c(\eta) r_c(\eta) I(\eta))\right]^{1/3}$  is a characteristic diameter. Eq. (3.3) has the solution  $x = W[(D/D_0)^3]$  where  $W$  is

the Lambert function. Substituting Eq. (3.3) into Eq. (3.1) and integrating gives:

$$L = \left(\frac{\Lambda}{D}\right)^2 W \left[ \left(\frac{D}{D_0}\right)^3 \right] H \quad (3.4)$$

where  $\Lambda = 2\lambda_s / \sqrt{i_c(\eta)}$  is a normalized collection length. Eq. (3.4) can be approximated in two limiting cases. First, the diffusion-limited growth regime follows from Eq. (3.4) for high supersaturation and a fast nucleation process ( $x \gg 1$ ), which leads to a logarithmic asymptote of the Lambert function:

$$L \cong \left(\frac{\Lambda}{D}\right)^2 \left[ 3 \ln \left(\frac{D}{D_0}\right) - \ln \left( \ln 3 \left(\frac{D}{D_0}\right) \right) \right] H, D \gg D_0 \quad (3.5)$$

Eq. (3.5) describes the conventional  $1/D^2$  behaviour of the length for small  $D_0$ , neglecting a weak logarithmic dependence, as is typically observed in nanowire growth.

In the second growth regime, nucleation-limited growth occurs for  $x \ll 1$  where  $x = W(z) \sim z$ . The  $L(D)$  relationship is then described by:

$$L \cong \frac{\Lambda^2 D}{D_0^3} H, D \ll D_0 \quad (3.6)$$

This results in the unusual, direct length dependence for large  $D_0$  where the supersaturation is low, and the decreased nucleation rate suppresses the nanowire growth of smaller diameters.

It is noteworthy that the well-known Gibbs-Thomson effect of the elevation of chemical potential in a droplet due to small diameter and higher

curvature [39, 40] is disregarded here since it is absent in the experimental  $L(D)$  curves even at small doping levels; the measured dependences are decreasing for all  $D$ . A small Be concentration at the droplet surface seems insufficient to cause such a significant increase in surface energy as to dramatically convert the diffusion-like  $L(D)$  relationship. With the Gibbs-Thomson modification included, the  $L(D)$  curves would start from a certain minimum diameter rather than from zero at small  $D$ . The corresponding generalization of the model will be presented elsewhere.

We hypothesize that the steady-state chemical potential of adatoms (and the corresponding supersaturation in the droplet) increases with Be doping. Applying Eqs. (3.3) and (3.4), this results in a decrease of the supersaturation  $\eta$ , a drastic decrease in the nucleation rate  $I(\eta)$ , and a rapidly increasing  $D_0$ . Lines in Figure 3.3 and Figure 3.5 present theoretical fits to the experimental data obtained from Eq. (3.4), with the parameters summarized in Table 3-II. In the model,  $D_0$  increases with Be concentration as discussed above, and the rapid increase of  $D_0$  from 3 nm for undoped samples to 78-145 nm at  $2\text{-}4 \times 10^{19} \text{ cm}^{-3}$  is attributed to a nucleation rate threshold dependent on supersaturation. The normalized collection length  $\Lambda$  is proportional to the value of  $1/\sqrt{i_c(\eta)}$  and should also increase as the supersaturation decreases, although slower than  $D_0$ . The significant increase from  $\Lambda = 28\text{-}50$  nm for undoped nanowires to  $\Lambda = 230\text{-}253$  nm for highly doped nanowires ( $2\text{-}4 \times 10^{19} \text{ cm}^{-3}$ ) obtained from our fits may be the result of secondary

effects of the growth rate suppression, such as decreased competition among nanowires or a reduction in shadowing effects for adatom collection length [11]. More complex growth effects such as the negative growth of the narrowest nanowires contributing to the growth of wider ones are also possible factors [40].

Table 3-II: Fitting parameters

Sample	Nominal Carrier		
	Concentration by Be	$D_0$ (nm)	$\Lambda$ (nm)
	Doping ( $\text{cm}^{-3}$ )		
A1	undoped	3	28
A2	$10^{18}$	22	45
A3	$2 \times 10^{19}$	145	230
B1	undoped	3	50
B2	$4 \times 10^{19}$	78	253

### 3.5 Chapter Summary

In conclusion, we have shown the transition following increased Be doping of InP nanowires from a diffusion-limited regime, displaying an inverse relationship between growth rate and diameter, to one that is instead almost linear or saturated. At high doping levels, this saturated  $L(D)$  relationship is most likely associated with the low nucleation rate of each monolayer, which suppresses the

growth rate of small diameter nanowires relative to larger diameter nanowires. Although demonstrated here for Au-catalyzed InP nanowires, we expect that this growth mechanism may also be present in other nanowire materials and growth methods, such as self-catalyzed nanowires. However, the extent to which they would display this phenomenon would depend on the chemical potential values of each system.

## **Chapter 4**

### **Compositional Characterization**

#### **4.1 Introduction**

Secondary ion mass spectrometry (SIMS) is an interesting technique in nanowire research for verifying the material composition along the axial direction. In particular, the incorporation of relatively small amounts of materials (such as dopants) in the nanowire growth system is not yet fully understood. In this chapter, a SIMS analysis of Be-doped InP nanowires is presented. The carrier concentrations of the samples were calculated using a calibration to a thin film reference sample, and the results are discussed in comparison with the nominal doping values.

#### **4.2 Experimental Details**

InP nanowire samples were prepared as described in Section 2.2, with MBE growth conditions summarized in Table 4-I (note that A1, A2, and A3 are the same samples as previously described in Section 3.2). All samples were grown at a V/III flux ratio of 5.6, a temperature of 420°C and an In impingement rate of 0.5  $\mu\text{m}/\text{h}$ . Nanowire arrays were prepared as SIMS specimens via the cyclotene spin-coating method described in Section 2.4.

As a calibration standard for the nanowires, a thin film reference of known doping concentration was also analyzed. The standard was an InP thin film doped with Be, and with a p-type carrier concentration measured by Hall effect between  $7 \times 10^{18} \text{ cm}^{-3}$  and  $8 \times 10^{18} \text{ cm}^{-3}$ , and taken as  $7.5 \times 10^{18} \text{ cm}^{-3}$ .

Surface Science Western acquired the raw data by measuring the average count rate for each element over brief, sequential time periods until the InP wafer substrate was reached. This point was identified by a rapid increase in In and P count rates, accompanied by a drop in beryllium count rate. The time scale was then converted into depth values by SEM measurement of each cyclotene film.

Table 4-I: Nanowire growth conditions

Sample	Structure	Nominal carrier concentration
		by Be doping ( $\text{cm}^{-3}$ )
A1	InP (30 min)	Undoped
A4	InP (30 min)	$1 \times 10^{17}$
A2	InP (30 min)	$1 \times 10^{18}$
A3	InP (30 min)	$2 \times 10^{19}$

### 4.3 Results

The count rates for the thin film reference are shown in Figure 4.1. From this data, the ratio of Be and In count rates within the thin film depth (0.75  $\mu\text{m}$ ) averaged  $0.0010 \pm 0.0003$ . This ratio was used when calibrating the nanowire dopant concentrations with the reference to account for volume variations.

It is important to note that the thin film reference value of  $p = 7.5 \times 10^{18} \text{ cm}^{-3}$  was measured by Hall effect, and is thus the activated carrier concentration  $N_A^-$ , not the physical dopant density  $N_A$ . The two values are related by the dopant ionization equation [41]:

$$N_A^- = \frac{N_A}{1 + g_A \exp[(E_A - E_F)/kT]} \quad (4.1)$$

where  $N_V$  is the effective density of states in the valence band,  $E_A$  is the acceptor energy level, and  $g_A$  is the ground-state degeneracy. These materials-specific parameters are presented in Table 4-II.

Eq. (4.1) can be expanded as:

$$N_A^- = \frac{N_A}{1 + g_A \exp\left[\frac{E_A - E_V}{kT} + \frac{E_V - E_F}{kT}\right]} \quad (4.2)$$

where  $E_V$  is the energy of the valence band. Assuming that the carrier concentration  $N_A^-$  is equivalent to the hole density:

$$p = N_V \frac{2}{\sqrt{\pi}} F_{1/2}(\eta) \quad (4.3)$$

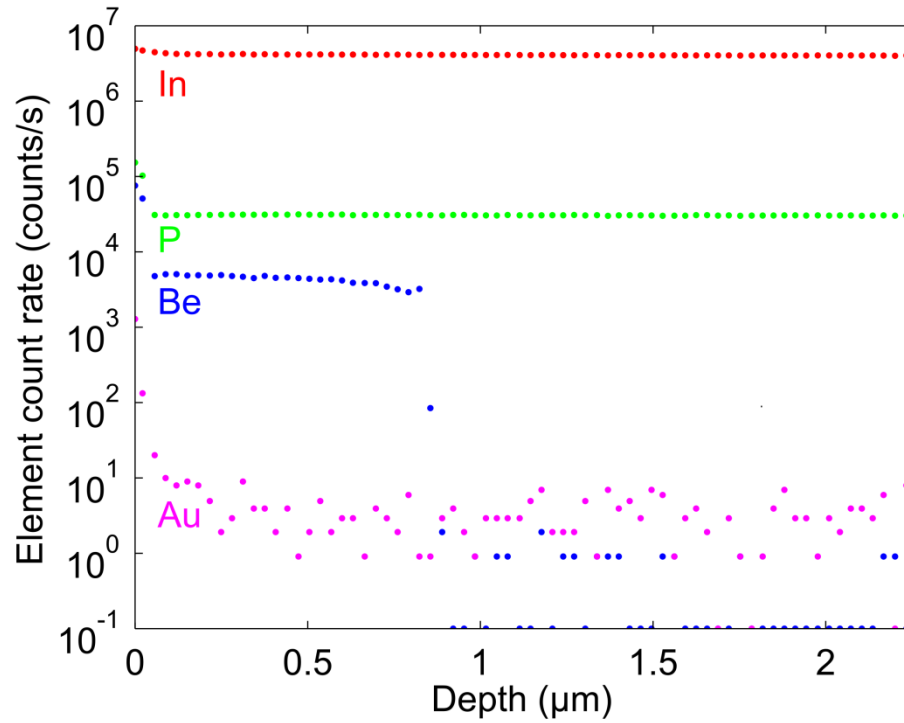


Figure 4.1: Element count rate for the reference thin film InP standard.

Table 4-II: InP material parameters

Parameter	Value
$E_A$ , ionization energy of Be in InP [42]	0.03 eV
$N_V$ , effective density of states in the InP valence band [43]	$1.1 \times 10^{19} \text{ cm}^{-3}$
$g_A$ , the ground state degeneracy of the valence band [41]	4

where  $F_{1/2}(\eta)$  is the Fermi-Dirac integral. Eq. (4.3) can then be equated to Eq. (4.2) and we obtain:

$$N_V \frac{2}{\sqrt{\pi}} F_{1/2}(\eta) = \frac{N_A}{1 + g_A \exp\left[\frac{E_A - E_V}{kT} + \frac{E_V - E_F}{kT}\right]} \quad (4.4)$$

This can be simplified using the Bednarczyk approximation [44]:

$$F_{1/2}(\eta) \approx \frac{1}{2} \sqrt{\pi} \left[ \frac{3}{4} \sqrt{\pi} a^{-3/8}(\eta) + \exp(-\eta) \right]^{-1} \quad (4.5)$$

where  $a(\eta) = \eta^4 + 33.6\eta\{1 - 0.68 \exp[-0.17(\eta + 1)^2]\} + 50$  and  $\eta = \frac{E_V - E_F}{kT}$ .

A Matlab zero-finding code was used to determine  $\frac{E_V - E_F}{kT}$ , and subsequently a numerical value for the reference doping concentration of  $N_{Aref} = 9 \times 10^{19} \text{ cm}^{-3}$ .

SIMS data obtained for the NW samples is displayed in Figure 4.2. The count rate of each sample was converted to a doping density  $N_{ANW}$  using the simple relation:

$$\frac{N_{ANW}}{N_{Aref}} = \frac{R_{NW}}{R_{ref}} \quad (4.6)$$

where  $N_{Aref} = 9 \times 10^{19} \text{ cm}^{-3}$  and  $R_{ref} = 1 \times 10^{-3}$  are the dopant density and the Be:In ratio of the thin film sample, respectively, and  $R_{NW}$  is the Be:In ratio of the nanowire sample.  $R_{NW}$  was calculated with count rates obtained near the substrate, where the density of nanowires was highest.

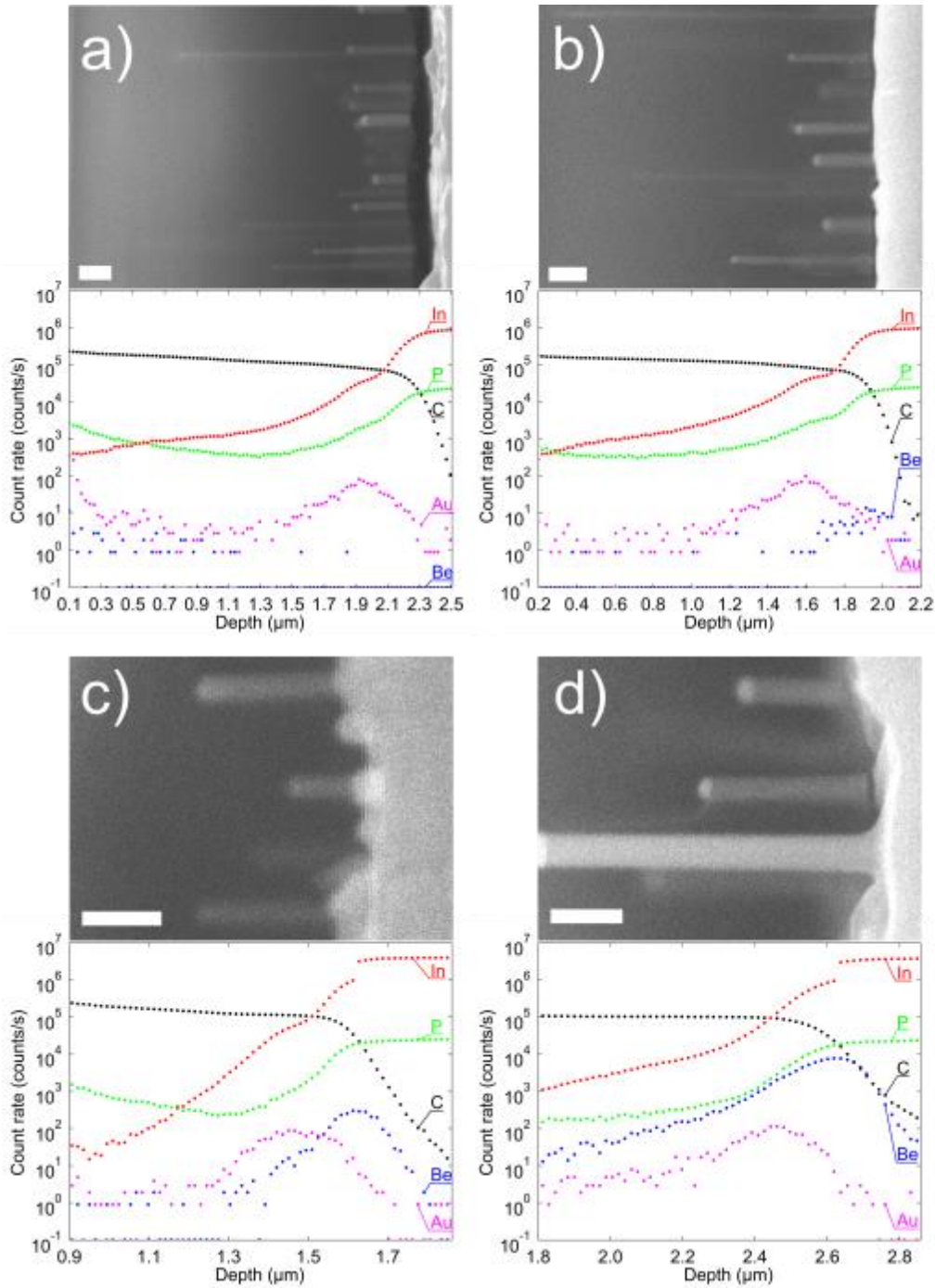


Figure 4.2: Cross-sectional SEM images and corresponding SIMS data of counts per second as a function of depth for nanowire arrays a) A1, b) A4, c) A2, and d) A3. Scale bars in the SEM images represent 2 μm. The values of 10<sup>-1</sup> are a proxy for ‘0’ on the log scale.

Table 4-III: Count rates near substrate

Sample	Depth ( $\mu\text{m}$ )	In rate (counts/s)	Be rate (counts/s)
A1	2.203	438100	0
A4	1.931	668200	12
A2	1.597	828400	256
A3	2.603	857100	7543

Table 4-IV: Nominal and measured carrier concentrations near substrate

Sample	Nominal $N_A^-$ ( $\text{cm}^{-3}$ )	Measured $N_A^-$ ( $\text{cm}^{-3}$ )
A1	Undoped	$0 - 5.1 \times 10^{17}$
A4	$1 \times 10^{17}$	$6.3 \times 10^{17} - 9.9 \times 10^{17}$
A2	$1 \times 10^{18}$	$4.2 \times 10^{18} - 4.2 \times 10^{18}$
A3	$2 \times 10^{19}$	$1.9 \times 10^{19} - 1.9 \times 10^{19}$

The count rate values (and depths at which they were measured) used for each sample are provided in Table 4-III. A range of values was calculated for the carrier concentration  $N_A^-$  based on an absolute error of  $\pm 4$  Be counts/s. This error value is the maximum Be count rate measured in sample A1, an undoped sample that should have measured no Be counts. These calculated ranges are thus presented with upper and lower bounds in Table 4-IV, alongside the nominal values.

#### 4.4 Discussion

Examining the count rates of the samples in Figure 4.2, there is a clear rise in In, P, and Be count rates as the NW density increases with depth. Note that the count rates are not directly quantitative (hence the need for a calibration reference), and elements present in equal quantities (In, P) may not be counted in equal numbers due to ion beam sensitivity. The onset of substrate measurements is identified by a sharp rise in In and P count rates, with a simultaneous drop in the carbon count rates (carbon is from the cyclotene filling medium). The beryllium counts should rapidly fall once the substrate is reached, but knock-on effects may prolong the decline (as seen in the thin film reference sample where the Be count rate drops over a width of ~60 nm, shown in Figure 4.1). Table 4-III clearly shows the expected progressive increase with Be count rates from sample A1 (undoped), through A4 ( $10^{17} \text{ cm}^{-3}$ ), A2 ( $10^{18} \text{ cm}^{-3}$ ), and A3 ( $2 \times 10^{19} \text{ cm}^{-3}$ ). As discussed, the count rate values (which measure dopant concentrations) were converted to carrier concentrations using Eqs. (4.3) and (4.6), with data obtained near the substrate of each sample.

Table 4-IV shows the agreement in orders of magnitude between the intended and calculated carrier concentrations. However, the agreement is noticeably better for A2 and A3 compared to A1 and A4. Samples A2 and A3 have nominal carrier concentrations more closely approximating that of the reference standard, making for a better comparison. Most significantly, exact  $N_A^-$  values calculated for samples A1 and A4 are not very reliable due to the

limitations of small count statistics. This also accounts for the much wider range of calculated values for A1 and A4. In contrast, working with  $10^2 - 10^3$  counts/s in samples A2 and A3 provides a more accurate representation of carrier concentrations, as shown in Figure 4.3. Qualitatively, the progression in Be count rates among the samples demonstrates the increased incorporation with higher doping.

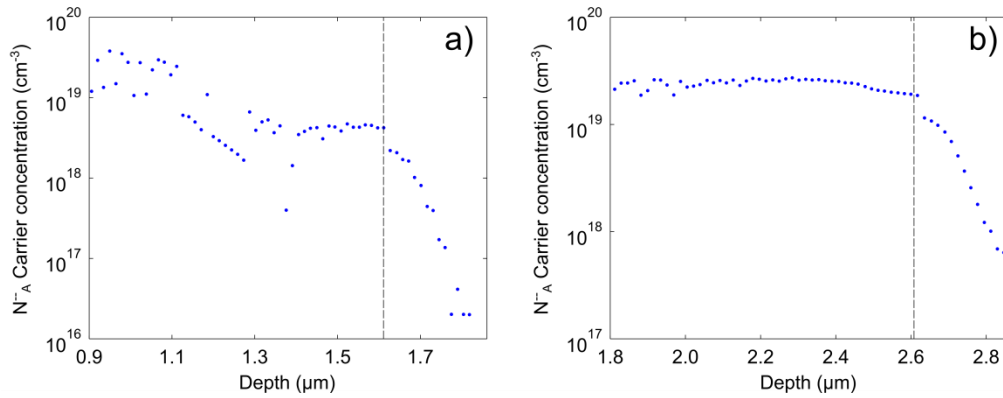


Figure 4.3: Carrier concentration as a function of depth for samples a) A2 and b) A3.

## 4.5 Chapter Summary

Four InP NW samples (undoped, and Be-doped at  $10^{17} \text{ cm}^{-3}$ ,  $10^{18} \text{ cm}^{-3}$ , and  $2 \times 10^{19} \text{ cm}^{-3}$ ) were analyzed by SIMS and clearly showed a qualitative rise in Be count rates with increased doping. The quantitative values of  $N_A^-$  determined for the highly-doped samples A2 and A3 were in good agreement with the intended carrier concentrations, but samples A1 and A4 had wider ranges

resulting from their low counts. However, the orders of magnitude calculated for carrier concentrations agreed with those of the nominal values for all samples.

## Chapter 5

### Optical Characterization Analysis

#### 5.1 Introduction

Several techniques to characterize the optoelectronic properties of semiconductors exist, but the small dimensions of nanowires can make contacting a challenge. Micro-photoluminescence ( $\mu$ PL) is a contact-free method, making it well suited for nanowire study and a useful complement to the compositional characterization discussed in Chapter 4. While SIMS provides information on the dopant density of a sample,  $\mu$ PL reveals how many of those dopants are activated and contributing to the carrier concentration (recall that in Chapter 4 the carrier concentrations discussed were inferred from the physical counts measured).

The energy spectra measured by  $\mu$ PL experiments exhibit the energy gaps characteristic of the band-to-band transitions within the semiconductor material. In a p-type material, the primary transitions are between the valence band, conduction band, and the acceptor level. In addition to these elementary levels, however, at high levels of doping (approximately  $>10^{18} \text{ cm}^{-3}$ ) impurity atoms can form a sub-band that results in a narrowing of the band gap. These and other effects on the PL spectra will be discussed in the interpretation of results.

## 5.2 Experimental Details

The PL experiments presented here were performed on InP nanowires from the same four samples analyzed by SIMS and discussed in Chapter 4 (of which samples A1, A2, and A3 were also discussed in Chapter 3). The growth conditions are summarized in Table 5-I, and the V/III flux ratio was 5.6 for all samples. Samples grew at a temperature of 420°C and In impingement rate of 0.5  $\mu\text{m}/\text{h}$ . Specimens were prepared by the sonication method with silicon substrates, as described in Section 2.5.

Prior to loading in the PL system, the specimens were examined by optical microscopy to identify regions of appropriately positioned nanowires, and referenced to scribe marks on the surface. Once loaded in the PL system, the CCD display enabled alignment with the nanowires previously mapped.

Samples were cooled by the cryostat to temperatures between 10 K and 20 K to minimize lattice vibrations and thermal effects. After positioning the laser spot, automated software was used to set the wavelength range (750 nm – 950 nm) and collection time (typically 20-30s, or longer for weak signals) for the spectrometer.

Table 5-I: Nanowire growth conditions

Sample	Structure	Nominal carrier concentration
		by Be doping ( $\text{cm}^{-3}$ )
A1	InP (30 min)	Undoped
A4	InP (30 min)	$1 \times 10^{17}$
A2	InP (30 min)	$1 \times 10^{18}$
A3	InP (30 min)	$2 \times 10^{19}$

### 5.3 Results

Measurements were taken from 11-13 nanowires for each sample, and representative spectra from the four samples are shown in Figure 5.1. The distribution of nanowire peak energies for each of the samples is shown in Figure 5.2. Among the four samples, there are two main emissions: Emission A, between 1.49-1.50 eV (827-832 nm) and Emission B (1.45-1.46 eV). Additionally, for the highest-doped sample A3, the majority of nanowires luminesced between 1.41-1.44 eV. The associated band transitions for these emissions, and considerations for other factors affecting the luminescence are discussed below.

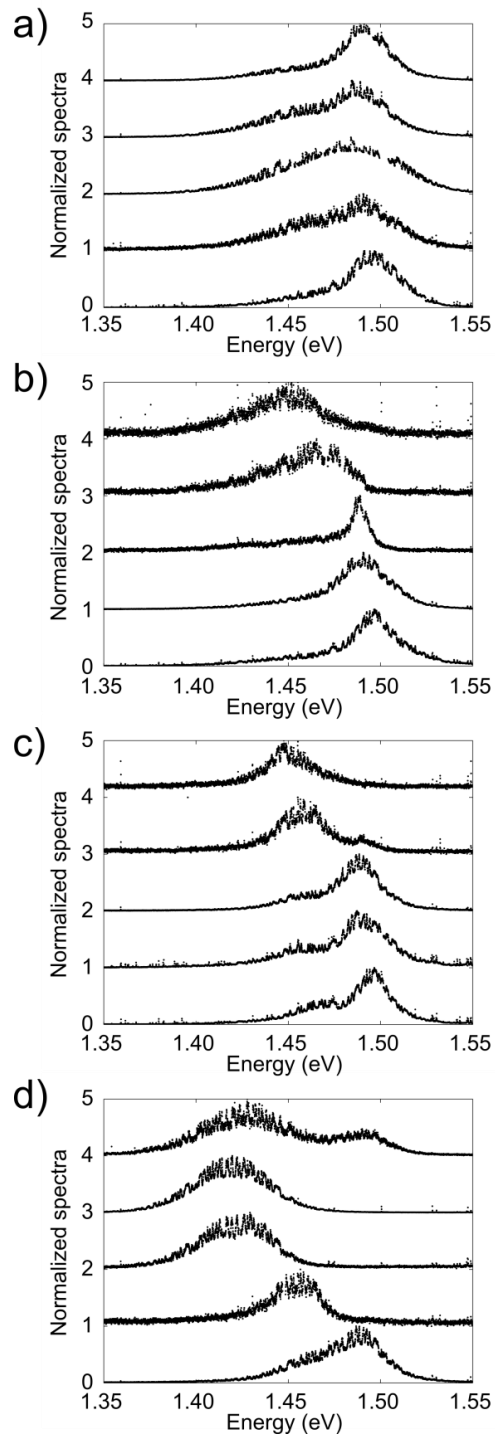


Figure 5.1: Representative spectra from a) sample A1, undoped, b) sample A4, Be doping= $10^{17} \text{ cm}^{-3}$ , c) sample A2, Be doping= $10^{18} \text{ cm}^{-3}$ , and d) sample A3, Be doping= $2 \times 10^{19} \text{ cm}^{-3}$ . Each spectrum is normalized to its dominant peak.

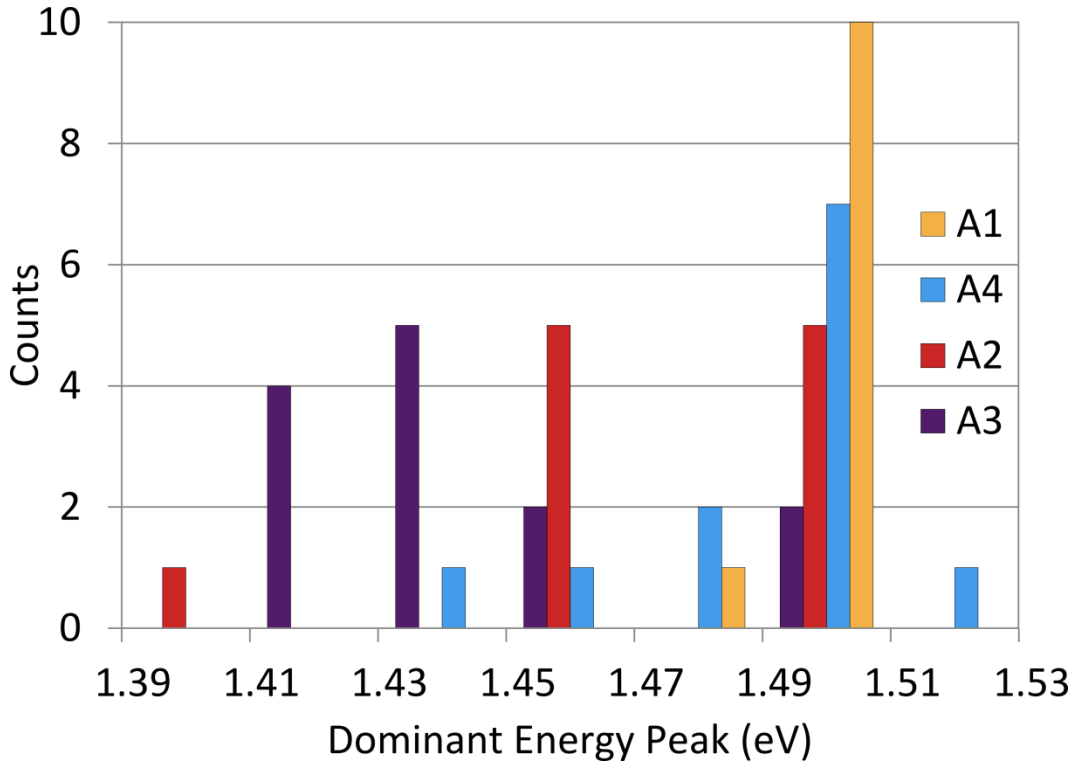


Figure 5.2: Distribution of the dominant peak energies emitted by the Be-doped InP nanowires (sample A1: undoped, sample A4:  $10^{17} \text{ cm}^{-3}$ , sample A2:  $10^{18} \text{ cm}^{-3}$ , sample A3:  $2 \times 10^{19} \text{ cm}^{-3}$ ).

### 5.4 Discussion

In general, Figure 5.2 shows the transition to lowered energies emitted by the samples as the p-doping level increases. Emission A (1.49-1.50 eV), the largest energy emitted, is assumed to be the conduction band to valence band transition. Bulk InP typically luminesces at a lower energy of 1.34-1.35 eV; however, it is zincblende in structure, compared to the wurtzite form often taken by nanowires. Other reported studies of wurtzite InP nanowires describe peak energies between 1.48-1.50 eV [24, 45–48]; thus Emission A is consistent with other reported bandgap values for InP nanowires. Additionally, effects of

quantum confinement are omitted here due to the larger diameter sizes measured and the lack of surface passivation. The Burstein-Moss effect, which results in an apparent widening of the bandgap due to the filling of states, is also disregarded due to the light effective mass of the holes (compared to electrons and energy bands with higher curvature).

Emission B (1.45-1.46 eV) is the energy associated with transitions between the conduction band and the acceptor level, approximately 30-40 meV below Emission A. This is consistent with differences reported by Kawamura et al [42] and Agaev et al [49] in epitaxially grown, Be-doped thin film InP.

Sample A1 spectra uniformly exhibited Emission A as the dominant peak, as would be ideal for an intrinsic semiconductor with no trap states. For the doped samples, however, the increase in doping level resulted in a transition to lower emitted energies. Sample A4 was lightly doped, and exhibited few lower-energy emissions. Sample A2 PL was evenly split between Emissions A and B. Finally, the most highly doped sample exhibited a much lower energy emission range, between 1.41 eV and 1.44 eV. This is due to bandgap narrowing effects that occur at high doping levels ( $> 10^{18} \text{ cm}^{-3}$ ) where dopants experience increased interactions between the atoms and form a sub-band.

Jain and Roulston [50] developed a general expression predicting the band gap narrowing (BGN) in highly-doped semiconductors as a function of the normalized dopant spacing:

$$r_s = \frac{r_a}{a}, \quad (5.1)$$

where  $r_a$  is half of the average dopant spacing given by:

$$\frac{4\pi N r_a^3}{3} = 1 \quad (5.2)$$

and  $a$  is the Bohr radius:

$$a = \frac{0.53\epsilon}{m^*} \times 10^{-8} \text{ cm.} \quad (5.3)$$

The factors that influence the system's potential energy are the exchange energy of the majority carriers (hole-hole interactions), the correlation energy due to electron-hole interactions, and the interaction energy of the impurity atoms. Summarizing these factors, the expression for bandgap narrowing is given in Eq. 5.4, normalized by the Rydberg energy Eq. 5.5:

$$\frac{\Delta E_g}{R} = 1.83 \frac{\Lambda}{N_b^{1/3}} \frac{1}{r_s} + \frac{0.95}{r_s^{3/4}} + \left[ 1 + \frac{R_{min}}{R} \right] \frac{1.57}{N_b r_s^{3/2}} \quad (5.4)$$

$$R = \frac{13.6m^*}{\epsilon^2} \text{ eV.} \quad (5.5)$$

Table 5-II: InP material parameters for BGN calculation [51]

<b>Parameter</b>	<b>Value</b>
$\Lambda$ , the correction factor for anisotropy in the light and heavy hole valence bands	0.75
$N_b$ , the number of equivalent band valleys	2
$m_h^*$ , the normalized effective hole mass	0.6
$m_e^*$ , the normalized effective electron mass	0.077
$\epsilon$ , the dielectric constant	12.35

For the highly-doped samples A2 and A3, calculating  $\Delta E_g/R$  with the parameter values provided in Table 5-II predicts band gap narrowing by 28 meV and 73 meV, respectively. For sample A3, this is in good agreement with the 1.41-1.44 eV emission range that dominates the PL spectra  $\sim 0.07$  eV below Emission A. For sample A2 bandgap narrowing may also be present, but the predicted value overlaps with the acceptor level-associated Emission B, and it is difficult to distinguish the BGN.

## 5.5 Chapter Summary

Four samples with varied levels of Be-doping were investigated by  $\mu$ PL experiments. Emission A, associated with the valence band to conduction band transition, occurred at 1.49-1.50 eV in good agreement with other reports of wurtzite InP nanowires. A sub-band emission B in the doped samples (A4, A2,

and A3) was identified at 1.45-1.46 eV, and is associated with the Be acceptor level. This transition to lower energy emissions with higher doping is consistent with the increase in acceptor doping, and demonstrates that the dopants not only incorporated as was demonstrated by SIMS, but ionized as well.

Bandgap narrowing effects were calculated for samples A2 and A3, as 28 meV and 73 meV respectively. For sample A2 this bandgap narrowing was difficult to distinguish, but for sample A3 the bandgap narrowing was in good agreement with the majority of dominant energy peaks between 1.41 eV and 1.44 eV.

## Chapter 6

### Conclusions and Future Work

#### 6.1 Thesis Summary

A nanowire doping study was prepared, growing InP nanowire ensembles under identical conditions with the exception of varied concentrations of Be doping. SEM analysis of the length-diameter trends showed a transition from the  $1/D^2$  dependence of low-doped nanowires to a more linear or saturated dependence for higher concentrations. As a result, the growth rates of small diameter nanowires were suppressed while larger diameter nanowires remained relatively unchanged. TEM analysis revealed no change in stacking fault density, excluding any effects on crystal structure as the cause. To further investigate, two InAs/InP heterostructures were prepared: one with undoped InP and one with highly Be-doped InP. Measurement of the  $L(D)$  relationship for the InP segments replicated the two contrasting inverse and direct dependences. Additionally, the axial growth of both samples' segments demonstrated that any change in diffusion length was insufficient to explain the suppression of growth rate for small diameter nanowires. The cause was thus speculated to be an increase in the droplet chemical potential, introducing a barrier to nucleation made visible in the suppression of small diameter nanowire growth. A model accounting for both regimes of diffusion- and nucleation-limited growth was presented.

Further analysis was performed to better understand how the doping had incorporated in the nanowire structure. By spin-coating the nanowire ensembles with cyclotene they were transformed into a “bulk-like” material, suitable for depth profiling by SIMS. By using a thin film reference and the dopant ionization equation, the samples’ physical dopant densities and ionized carrier concentrations were inferred from the counts. The carrier concentrations of the higher-doped samples agreed closely with their nominal values, but for the lowest-doped samples the ranges determined were wide. This was due to the sensitivity to small count values inherent in the low doping. However, dopant counts qualitatively increased with higher nominal doping, and all calculated carrier concentration values agreed in order of magnitude with nominal values.

Finally, to investigate the activation of incorporated dopants, transitions within the bandgap were studied through  $\mu$ PL experiments. Nanowires were removed from the substrate by sonication and deposited on a silicon substrate before illuminating individually and measuring the luminesced wavelengths. Two main energy peaks were observed at 1.49-1.50 eV (Emission A) and 1.45-1.46 eV (Emission B); the difference between the two emissions was consistent with differences reported for epitaxially-grown undoped and Be-doped InP thin film samples. As nanowires with higher levels of doping were measured, the occurrence of Emission B compared to Emission A grew. This indicated an increase in activated dopants, and the formation of an acceptor level within the bandgap. Additionally, the highest-doped sample also exhibited lower band-to-

band peak energies of  $\sim 0.07$  eV compared to the undoped nanowires, consistent with theoretical BGN predictions.

## 6.2 Future Work

Although the characterization of the InP nanowire Be-doping study was extensive, there is still room for future work to complete our understanding of this and other doping systems. The  $\mu$ PL study indicated progressive increases in ionization with increased doping levels, but it would be valuable to confirm the carrier concentrations through current-voltage (IV) experiments. Additionally, this would verify the carrier concentrations inferred from the dopant densities measured by SIMS. More precise measurement of the electrical properties would require new samples grown on highly conductive p-type wafers for measurement of IV curves. This would produce a resistor-like ensemble that could be interpreted using the model of nanowire conductivity published by Chia and LaPierre, taking into account the dependence of depletion on doping level [29].

Other dopants and nanowire compositions should also be investigated to form a more complete understanding of the interactions in different material systems, particularly for device design. Preliminary studies have already been performed for InP doped with silicon and tellurium (Figure 6.1). Highly Si-doped InP nanowires grown under otherwise identical conditions to the samples in this thesis showed a strongly inverse (diffusion-limited)  $L(D)$  dependence. Highly Te-doped wires, however, resulted in a dramatic suppression of growth, and by

preparing a systematic doping study it may be possible to observe at which doping concentration this onset occurs. Other systems of nanowires may be likewise affected by doping in unexpected ways, and by further study these regimes and their causes may be better understood.

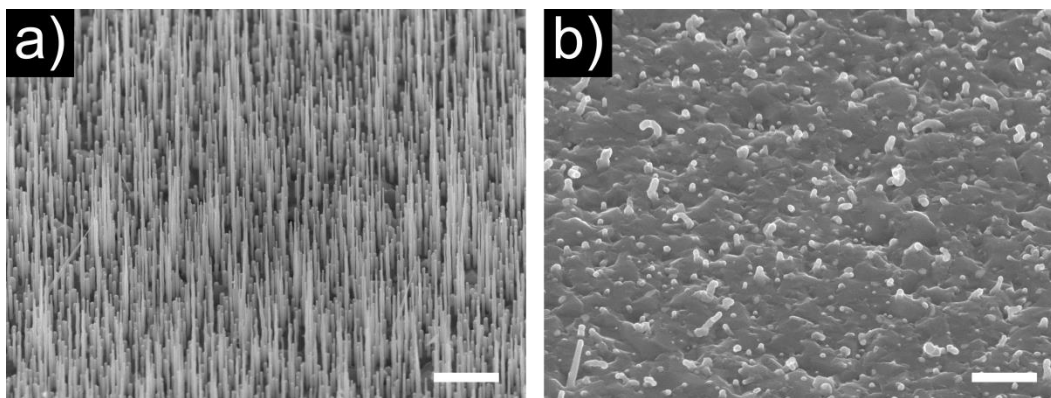


Figure 6.1: Tilted views ( $45^\circ$ ) of InP nanowires doped with a) silicon and b) tellurium. Scale bars indicate  $1\ \mu\text{m}$ .

It is my hope that the information summarized and interpreted here, as well as further research it may inspire, will contribute to the toolbox of knowledge used for nanowire device design and growth in the future.

## References

- [1] G. E. Moore, "Cramming more components onto integrated circuits, Reprinted from Electronics, volume 38, number 8, April 19, 1965, pp.114 ff.," *IEEE Solid-State Circuits Newsletter*, vol. 20, no. 3, pp. 33–35, Sep. 2006.
- [2] R. P. Feynman, "There's plenty of room at the bottom: An invitation to enter a new field of physics," *Engineering and Science*, vol. 23, no. 5, pp. 22–35, 1960.
- [3] R. S. Wagner and W. C. Ellis, "Vapor-Liquid-Solid Mechanism of Single Crystal Growth," *Applied Physics Letters*, vol. 4, no. 5, p. 89, 1964.
- [4] F. C. Frank, "The influence of dislocations on crystal growth," *Discussions of the Faraday Society*, vol. 5, no. 48, p. 48, Jan. 1949.
- [5] E. Givargizov, "Fundamental aspects of VLS growth," *Journal of Crystal Growth*, vol. 31, pp. 20–30, Dec. 1975.
- [6] V. Dubrovskii, N. Sibirev, G. Cirlin, I. Soshnikov, W. H. Chen, R. Larde, E. Cadel, P. Pareige, T. Xu, B. Grandidier, J.-P. Nys, D. Stievenard, M. Moewe, L. Chuang, and C. Chang-Hasnain, "Gibbs-Thomson and diffusion-induced contributions to the growth rate of Si, InP, and GaAs nanowires," *Physical Review B*, vol. 79, no. 20, pp. 1–7, May 2009.
- [7] J. Johansson, C. P. T. Svensson, T. Mårtensson, L. Samuelson, and W. Seifert, "Mass transport model for semiconductor nanowire growth.," *The journal of physical chemistry. B*, vol. 109, no. 28, pp. 13567–71, Jul. 2005.
- [8] F. Glas, J. Harmand, and G. Patriarche, "Why Does Wurtzite Form in Nanowires of III-V Zinc Blende Semiconductors?," *Phys. Rev. Lett.*, vol. 146101, no. October, pp. 3–6, 2007.
- [9] M. Plante and R. Lapierre, "Growth mechanisms of GaAs nanowires by gas source molecular beam epitaxy," *Journal of Crystal Growth*, vol. 286, no. 2, pp. 394–399, Jan. 2006.
- [10] M. C. Plante, "Metal-Assisted Growth of III-V Nanowires by MBE," McMaster University, 2009.

- [11] N. V. Sibirev, M. Tchernycheva, M. a. Timofeeva, J.-C. Harmand, G. E. Cirlin, and V. G. Dubrovskii, "Influence of shadow effect on the growth and shape of InAs nanowires," *Journal of Applied Physics*, vol. 111, no. 10, p. 104317, 2012.
- [12] V. Dubrovskii and N. Sibirev, "Growth rate of a crystal facet of arbitrary size and growth kinetics of vertical nanowires," *Physical Review E*, vol. 70, no. 3, pp. 1–7, Sep. 2004.
- [13] V. G. Dubrovskii, G. E. Cirlin, N. V Sibirev, F. Jabeen, J. C. Harmand, and P. Werner, "New mode of vapor-liquid-solid nanowire growth.," *Nano letters*, vol. 11, no. 3, pp. 1247–53, Mar. 2011.
- [14] V. G. Dubrovskii, G. E. Cirlin, and V. M. Ustinov, "Semiconductor nanowhiskers: Synthesis, properties, and applications," *Semiconductors*, vol. 43, no. 12, pp. 1539–1584, Dec. 2009.
- [15] P. Krogstrup, H. I. Jørgensen, E. Johnson, M. H. Madsen, C. B. Sørensen, A. F. i Morral, M. Aagesen, J. Nygård, and F. Glas, "Advances in the theory of III–V nanowire growth dynamics," *Journal of Physics D: Applied Physics*, vol. 46, no. 31, p. 313001, Aug. 2013.
- [16] H.-M. Kim, Y.-H. Cho, H. Lee, S. Il Kim, S. R. Ryu, D. Y. Kim, T. W. Kang, and K. S. Chung, "High-Brightness Light Emitting Diodes Using Dislocation-Free Indium Gallium Nitride/Gallium Nitride Multiquantum-Well Nanorod Arrays," *Nano Letters*, vol. 4, no. 6, pp. 1059–1062, Jun. 2004.
- [17] T. Bryllert, L.-E. Wernersson, T. Löwgren, and L. Samuelson, "Vertical wrap-gated nanowire transistors," *Nanotechnology*, vol. 17, no. 11, pp. S227–S230, Jun. 2006.
- [18] J. A. Czaban, D. A. Thompson, and R. R. LaPierre, "GaAs core--shell nanowires for photovoltaic applications.," *Nano letters*, vol. 9, no. 1, pp. 148–54, Jan. 2009.
- [19] R. R. LaPierre, A. C. E. Chia, S. J. Gibson, C. M. Haapamaki, J. Boulanger, R. Yee, P. Kuyanov, J. Zhang, N. Tajik, N. Jewell, and K. M. A. Rahman, "III-V nanowire photovoltaics: Review of design for high efficiency," *physica status solidi (RRL) - Rapid Research Letters*, p. n/a–n/a, Apr. 2013.

- [20] M. Lee, K. Y. Baik, M. Noah, Y. Kwon, J. Lee, and S. Hong, "Nanowire and nanotube transistors for lab-on-a-chip applications.," *Lab on a chip*, vol. 9, no. 16, pp. 2267–80, Aug. 2009.
- [21] X. Chen, C. K. Y. Wong, C. A. Yuan, and G. Zhang, "Nanowire-based gas sensors," *Sensors and Actuators B: Chemical*, vol. 177, pp. 178–195, Feb. 2013.
- [22] K. L. Kavanagh, "Misfit dislocations in nanowire heterostructures," *Semiconductor Science and Technology*, vol. 25, no. 2, p. 024006, Feb. 2010.
- [23] R. E. Algra, M. a Verheijen, M. T. Borgström, L.-F. Feiner, G. Immink, W. J. P. van Enkevort, E. Vlieg, and E. P. a M. Bakkers, "Twinning superlattices in indium phosphide nanowires.," *Nature*, vol. 456, no. 7220, pp. 369–72, Nov. 2008.
- [24] J. Wallentin, K. Mergenthaler, M. Ek, L. R. Wallenberg, L. Samuelson, K. Deppert, M. Pistol, and M. T. Borgström, "Probing the wurtzite conduction band structure using state filling in highly doped InP nanowires.," *Nano letters*, vol. 11, no. 6, pp. 2286–90, Jun. 2011.
- [25] M. T. Borgström, E. Norberg, P. Wickert, H. a Nilsson, J. Trägårdh, K. a Dick, G. Statkute, P. Ramvall, K. Deppert, and L. Samuelson, "Precursor evaluation for in situ InP nanowire doping.," *Nanotechnology*, vol. 19, no. 44, p. 445602, Nov. 2008.
- [26] M. Hilse, M. Ramsteiner, S. Breuer, L. Geelhaar, and H. Riechert, "Incorporation of the dopants Si and Be into GaAs nanowires," *Applied Physics Letters*, vol. 96, no. 19, p. 193104, 2010.
- [27] L. Rigutti, A. De Luna Bugallo, M. Tchernycheva, G. Jacopin, F. H. Julien, G. Cirlin, G. Patriarche, D. Lucot, L. Travers, and J.-C. Harmand, "Si Incorporation in InP Nanowires Grown by Au-Assisted Molecular Beam Epitaxy," *Journal of Nanomaterials*, vol. 2009, pp. 1–7, 2009.
- [28] S. Wirths, K. Weis, A. Winden, K. Sladek, C. Volk, S. Alagha, T. E. Weirich, M. von der Ahe, H. Hardtdegen, H. Lüth, N. Demarina, D. Grützmacher, and T. Schäpers, "Effect of Si-doping on InAs nanowire transport and morphology," *Journal of Applied Physics*, vol. 110, no. 5, p. 053709, 2011.

- [29] A. C. E. Chia and R. R. LaPierre, "Analytical model of surface depletion in GaAs nanowires," *Journal of Applied Physics*, vol. 112, no. 6, p. 063705, 2012.
- [30] R. J. Yee, S. J. Gibson, V. G. Dubrovskii, and R. R. LaPierre, "Effects of Be doping on InP nanowire growth mechanisms," *Applied Physics Letters*, vol. 101, no. 26, p. 263106, Dec. 2012.
- [31] C. M. Haapamaki, "Growth of InAs/InP Nanowires by Molecular Beam Epitaxy," McMaster University, 2013.
- [32] A. C. E. Chia, J. P. Boulanger, and R. R. LaPierre, "Unlocking doping and compositional profiles of nanowire ensembles using SIMS," *Nanotechnology*, vol. 24, no. 4, p. 045701, Feb. 2013.
- [33] S. A. Fortuna and X. Li, "Metal-catalyzed semiconductor nanowires: a review on the control of growth directions," *Semiconductor Science and Technology*, vol. 25, no. 2, p. 024005, Feb. 2010.
- [34] M. Plante and R. Lapierre, "Au-assisted growth of GaAs nanowires by gas source molecular beam epitaxy: Tapering, sidewall faceting and crystal structure," *Journal of Crystal Growth*, vol. 310, no. 2, pp. 356–363, Jan. 2008.
- [35] M. C. Plante and R. R. LaPierre, "Analytical description of the metal-assisted growth of III–V nanowires: Axial and radial growths," *Journal of Applied Physics*, vol. 105, no. 11, p. 114304, 2009.
- [36] C. M. Haapamaki and R. R. Lapierre, "Mechanisms of molecular beam epitaxy growth in InAs/InP nanowire heterostructures," *Nanotechnology*, vol. 22, no. 33, p. 335602, Aug. 2011.
- [37] V. G. Dubrovskii and N. V. Sibirev, "General form of the dependences of nanowire growth rate on the nanowire radius," *Journal of Crystal Growth*, vol. 304, no. 2, pp. 504–513, Jun. 2007.
- [38] V. G. Dubrovskii, N. V. Sibirev, J. C. Harmand, and F. Glas, "Growth kinetics and crystal structure of semiconductor nanowires," *Physical Review B*, vol. 78, no. 23, p. 235301, Dec. 2008.
- [39] L. E. Fröberg, W. Seifert, and J. Johansson, "Diameter-dependent growth rate of InAs nanowires," *Physical Review B*, vol. 76, no. 15, p. 153401, Oct. 2007.

- [40] V. Dubrovskii, N. Sibirev, G. Cirilin, A. Bouravleuv, Y. Samsonenko, D. Dheeraj, H. Zhou, C. Sartel, J. Harmand, G. Patriarche, and F. Glas, "Role of nonlinear effects in nanowire growth and crystal phase," *Physical Review B*, vol. 80, no. 20, p. 205305, Nov. 2009.
- [41] S. M. Sze and K. K. Ng, *Physics of Semiconductor Devices*, 3rd ed., vol. 9, no. 5. Hoboken: John Wiley & Sons, Inc., 2007, p. 22.
- [42] Y. Kawamura, H. Asahi, and H. Nagai, "Electrical and optical properties of Be-doped InP grown by molecular beam epitaxy," *Journal of Applied Physics*, vol. 54, no. 2, p. 841, 1983.
- [43] Y. A. Goldberg, "Gallium Indium Phosphide ( $\text{Ga}_x\text{In}_{1-x}\text{P}$ )," in in *Handbook Series on Semiconductor Parameters, Volume 2: Ternary and Quaternary III-V Compounds*, M. Levinshtein, S. Rumyantsev, and M. Shur, Eds. Singapore: World Scientific Pub. Co., Inc., 1999, p. 37.
- [44] D. Bednarczyk and J. Bednarczyk, "The approximation of the Fermi-Dirac integral 12 ( $\eta$ )," *Physics Letters A*, vol. 64, no. 4, pp. 409–410, Jan. 1978.
- [45] J. Bao, D. C. Bell, F. Capasso, J. B. Wagner, T. Mårtensson, J. Trägårdh, and L. Samuelson, "Optical properties of rotationally twinned InP nanowire heterostructures," *Nano letters*, vol. 8, no. 3, pp. 836–41, Mar. 2008.
- [46] A. Mishra, L. V. Titova, T. B. Hoang, H. E. Jackson, L. M. Smith, J. M. Yarrison-Rice, Y. Kim, H. J. Joyce, Q. Gao, H. H. Tan, and C. Jagadish, "Polarization and temperature dependence of photoluminescence from zincblende and wurtzite InP nanowires," *Applied Physics Letters*, vol. 91, no. 26, p. 263104, 2007.
- [47] K. Pemasiri, M. Montazeri, R. Gass, L. M. Smith, H. E. Jackson, J. Yarrison-Rice, S. Paiman, Q. Gao, H. H. Tan, C. Jagadish, X. Zhang, and J. Zou, "Carrier dynamics and quantum confinement in type II ZB-WZ InP nanowire homostructures," *Nano letters*, vol. 9, no. 2, pp. 648–54, Feb. 2009.
- [48] K. Ikejiri, Y. Kitauchi, K. Tomioka, J. Motohisa, and T. Fukui, "Zinc blende and wurtzite crystal phase mixing and transition in indium phosphide nanowires," *Nano letters*, vol. 11, no. 10, pp. 4314–8, Oct. 2011.
- [49] V. V. Agaev, I. N. Arsent'ev, S. G. Metreveli, S. P. Starosel'tseva, and G. I. Yablochkina, "Beryllium diffusion and influence on the luminescent and

electrical properties of indium phosphide,” *Technical Physics Letters*, vol. 32, no. 8, pp. 709–711, Aug. 2006.

- [50] S. C. Jain and D. J. Roulston, “A simple expression for band gap narrowing (BGN) in heavily doped Si, Ge, GaAs and  $GexSi_{1-x}$  strained layers,” *Solid-State Electronics*, vol. 34, no. 5, pp. 453–465, May 1991.
- [51] S. C. Jain, J. M. McGregor, and D. J. Roulston, “Band-gap narrowing in novel III-V semiconductors,” *Journal of Applied Physics*, vol. 68, no. 7, p. 3747, 1990.